Research Square

Preprints are preliminary reports that have not undergone peer review.
They should not be considered conclusive, used to inform clinical practice,
or referenced by the media as validated information.

Agreement between Sentinel-1 C-band backscatter change and Sentinel-2 burn severity indices across land-cover types in a low-biomass transitional eco-region

M Shahriar Sonet

sonet.m34@gmail.com

The University of Texas at Dallas https://orcid.org/0000-0002-2796-0752

Research Article

Keywords: Wildfire, microwave, Synthetic Aperture Radar (SAR), Geospatial Big Data, Wildland-Urban Interface (WUI)

Posted Date: October 23rd, 2026

DOI: https://doi.org/10.21203/rs.3.rs-11461959/v1

License: This work is licensed under a Creative Commons Attribution 4.0 International License.
Read Full License

Additional Declarations: The authors declare no competing interests.

Agreement between Sentinel-1 C-band backscatter change and Sentinel-2 burn severity indices across land-cover types in a low-biomass transitional eco-region

Abstract

The shifting fire regimes of the Southern Great Plains, characterized by increasing wildfire frequency and intensity, present challenges for traditional damage-assessment methods. Optical indices such as the Differenced Normalized Burn Ratio (dNBR) are standard for forested environments, but their efficacy is limited in the low-biomass, transitional eco-regions of Texas due to rapid herbaceous recovery and background soil signals. This study compares Sentinel-1 C-band Synthetic Aperture Radar (SAR) backscatter change ($\Delta\sigma^0$) with Sentinel-2 optical burn-severity indices (dNBR and RdNBR) to characterize biophysical alterations from the 2022 Eastland Complex Fire. Across the fire complex, only ~42% of the mapped perimeter was classified as burned, with substantial unburned refugia remaining. The cross-polarized (VH) backscatter change showed a wider dynamic range than the co-polarized (VV) signal, indicating greater sensitivity to structural loss. Radar backscatter change correlated more strongly with dNBR in evergreen forest ($r = -0.53$) than in shrub/scrub ($r = -0.29$) or grassland ($r = -0.19$), and RdNBR consistently underperformed dNBR as a proxy for radar-detected structural loss across all land-cover classes, suggesting that relativization amplifies noise in sparsely vegetated landscapes. A radar-derived moisture-loss index was spatially consistent with expected post-fire hydrological deficits, complementing optical indices in areas where they showed limited dynamic range. These findings support integrating active microwave remote sensing with optical indices for burn-severity assessment in semi-arid, transitional fire regimes.

Keywords: *Wildfire, microwave, Synthetic Aperture Radar (SAR), Geospatial Big Data, Wildland-Urban Interface (WUI)*

1. Introduction

Wildfires are among the most destructive natural hazards in the United States, and as climate conditions shift, they are occurring more frequently and burning with greater intensity. This trend represents a systemic change in fire behavior driven by human-induced climate change, long-standing land management decisions, and the expansion of the Wildland-Urban Interface (WUI). While wildfire research has historically focused on dense conifer forests in the Western U.S., recent events demonstrate a clear expansion of large fires into the Great Plains and the Southern United States, challenging long-held assumptions about extreme fire geography (Donovan et al., 2023).

The traditional fire season has evolved into a year-round phenomenon, driven by warmer temperatures, earlier spring snowmelt, and prolonged vapor pressure deficits (Westerling, 2016). These changes carry serious ecological and socio-economic consequences, threatening water resources and air quality at scales exceeding historical natural disturbances (Jaffe et al., 2020). This context is essential for understanding the 2022 Eastland Complex Fire in Texas, where extreme weather, accumulated fuels, and human ignition sources converged to produce a destructive event in a transitional eco-region.

Assessing wildfire damage is critical for managing regional ecosystem resilience. Over the past several decades, advances in geospatial technologies have revolutionized fire science, allowing researchers to rapidly assess fire extent and severity (Miller & Thode, 2007). While initial efforts utilized moderate-resolution sensors like Landsat and MODIS, the recent introduction of Sentinel-2 (multispectral) and Sentinel-1 (C-band Synthetic Aperture Radar) provides unprecedented detail. Sentinel-2 offers narrow-band coverage at red-edge and short-wave infrared (SWIR) wavelengths sensitive to canopy water and chlorophyll (Brown et al., 2018), while Sentinel-1 provides an all-weather perspective on structural alterations.

Despite these advances, standard optical indices like the Differenced Normalized Burn Ratio (dNBR) and its relative version (RdNBR) vary significantly in sensitivity across different ecosystems. In the heterogeneous landscapes of Texas where grasslands mix with oak motts and mesquite the spectral signal can be confounded by rapid post-fire herbaceous recovery and bright background soil signals (Yin et al., 2020). These limitations highlight the urgent need for a multi-sensor framework that integrates active microwave remote sensing to resolve the spectral-structural decoupling inherent in human-modified, semi-arid fire regimes.

Since the development of the Normalized Burn Ratio (NBR) by Key and Benson (2006), satellite remote sensing has been the primary tool for mapping fire perimeters. The difference between pre- and post-fire NBR (dNBR) provides a measure of change, while the Relative differenced NBR (RdNBR) was developed to correct pre-fire vegetation density (Miller et al., 2009). However, these indices face challenges in open canopies or shrublands, where background soil signals often overwhelm the vegetation signal (Soverel et al., 2010). Furthermore, rapid post-fire green-up in grassy fuels can mask woody mortality, leading to potential misclassification of fire effects (Picotte et al., 2020). To address these limitations, recent research has explored machine learning to integrate spectral indices with topographic and texture data for more robust classification (Hu et al., 2023). To overcome the atmospheric and biophysical limitations of optical sensors, active remote sensing is increasingly utilized. While LiDAR provides direct measurements of vegetation structure, its acquisition is often cost-prohibitive over large areas (Rahman & Rashed, 2015).

Synthetic Aperture Radar (SAR) offers a scalable alternative, where backscatter (intensity) changes based on surface roughness and moisture. Fire-driven removal of vegetation generally decreases volume scattering and increases surface scattering, though the magnitude depends on the radar wavelength (Tanase et al., 2010). C-band SAR (Sentinel-1) is particularly sensitive to canopy leaves and smaller branches, as well as the dielectric properties of the surface (Millard et al., 2022). This makes differential backscatter analysis (σ^0) a robust method for monitoring structural recovery and soil moisture memory, independent of cloud cover or smoke.

The Eastland Complex Fire of March 2022 serves as a critical case study for the shifting fire regimes of the Southern Great Plains, occurring in a transitional eco-region characterized by a heterogeneous mosaic of oak motts, mesquite shrublands, and mixed grasslands. Assessing ecological damage here is difficult because standard optical indices like the Differenced Normalized Burn Ratio (dNBR) were designed for dense forests. In the Texas Cross Timbers, rapid grass regrowth and high soil reflectance often interfere with these signals. This creates a risk where standard maps misclassify fire effects due to the fast recovery of herbaceous fuels. Synthetic Aperture Radar (SAR) provides an all-weather alternative sensitive to moisture and structure, but its use in Texas shrublands is not well documented. Without comparing active and passive sensors, managers lack a reliable way to quantify fire impact and plan restoration in these specific environments.

Current literature lacks SAR validation in transitional biomes. Most research focuses on high-biomass boreal or tropical forests rather than the grass-shrub savannas of Texas. Furthermore, the correlation between radar backscatter ($\Delta\sigma^0$) and optical indices across specific land covers remains uncertain. There is also a temporal disconnect in current assessments. SAR detects immediate structural loss, while optical sensors monitor greenness, which recovers quickly in grass-dominated systems. Integrating these observations is necessary to evaluate fire-induced change and recovery together.

This study evaluates combined optical and radar data to map burn severity and moisture loss. The work first quantifies severity distributions using Sentinel-2 indices. It then measures the sensitivity of Sentinel-1 C-band backscatter to combustion-driven changes in vegetation and moisture. A primary goal is to determine where radar serves as a reliable proxy for fire effects by analyzing correlations across different land covers. Finally, the study examines how slope and land use influenced observed burn patterns.

To guide this investigation, this study addresses several interrelated questions regarding the measurement and drivers of the Eastland Complex Fire. Fundamentally, the research asks how the spatial patterns of burn severity derived from Sentinel-2 optical indices (dNBR, RdNBR) compared to those derived from Sentinel-1 SAR backscatter changes ($\Delta\sigma^0$). It further investigates whether there is a statistically significant correlation between optical burn severity (dNBR) and radar backscatter loss ($\Delta\sigma^0_{VV}$ and $\Delta\sigma^0_{VH}$), and to what extent this correlation varies between grassland and shrubland ecosystems. From a methodological standpoint, the study questions whether the combination of VV and VH backscatter changes can serve as a reliable proxy for moisture and structure loss in areas where optical imagery might be compromised or ambiguous. Finally, regarding the physical drivers of the event, the research examines how local topographic

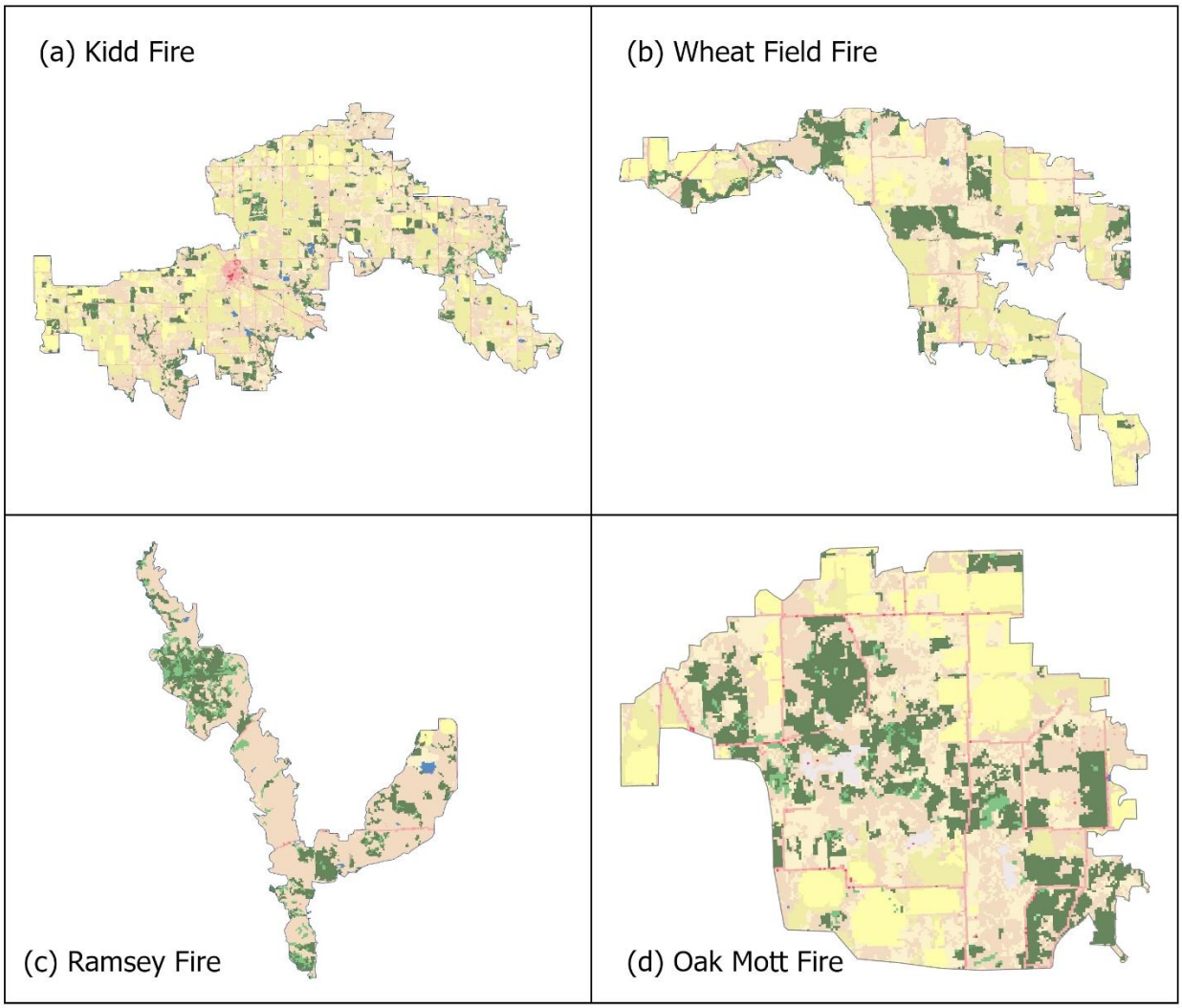
factors, such as slope, and pre-existing land cover classes influenced the ultimate severity of the Eastland Complex Fire.

This pattern is consistent with the broader intensification of drought cycles under anthropogenic climate change, which has increased vapor pressure deficit and fuel flammability across the Southern Great Plains (Williams et al., 2019; Lee et al., 2025). As vegetation becomes water-stressed, associated changes in dielectric properties are detectable via microwave remote sensing, linking fuel-moisture conditions directly to the radar-based methods used in this study (Mass & Ovens, 2024).

Finally, wildfires in the Southern Great Plains must be understood as tightly coupled socio-environmental systems. Unlike the lightning-dominated regimes of the Western U.S., fires in Texas are predominantly driven by human ignitions and land-use patterns. Specific socio-economic indicators, such as the expansion of the Wildland-Urban Interface (WUI) and infrastructure density, serve as significant predictors for fire risk (Katuwal & Kafley, 2024). Consequently, characterizing the 2022 Eastland Complex requires a multi-sensor approach that connects physical combustion effects with the underlying environmental and anthropogenic drivers that shape the regional fire landscape.

2. Study Area

The research focuses on the Eastland Complex Fire, which occurred in March 2022 in Central Texas. The analysis focuses on the four biggest fires, which burned during 16 March 2022 to 31 March 2022. The selected fires those were analyzed are Kidd fire, Wheatfield fire, Ramsey fire and Oak Mott fire (Figure 1). The complex consisted of multiple distinct ignitions but they falls into several counties namely Eastland, Callahan, Brown and Comanche county and burnt over 54,000 acres. Ecologically The region lies within the Cross Timbers and Rolling Plains ecoregions, a transitional zone characterized by a mosaic of vegetation types. The landscape is dominated by mixed oak woodlands (*Quercus* spp.), mesquite shrublands (*Prosopis glandulosa*) and mixed-grass prairies. This fuel complex is highly volatile, with fine grassy fuels facilitating rapid fire spread and woody vegetation contributing to higher residence times and severity (Katuwal & Kafley, 2024).



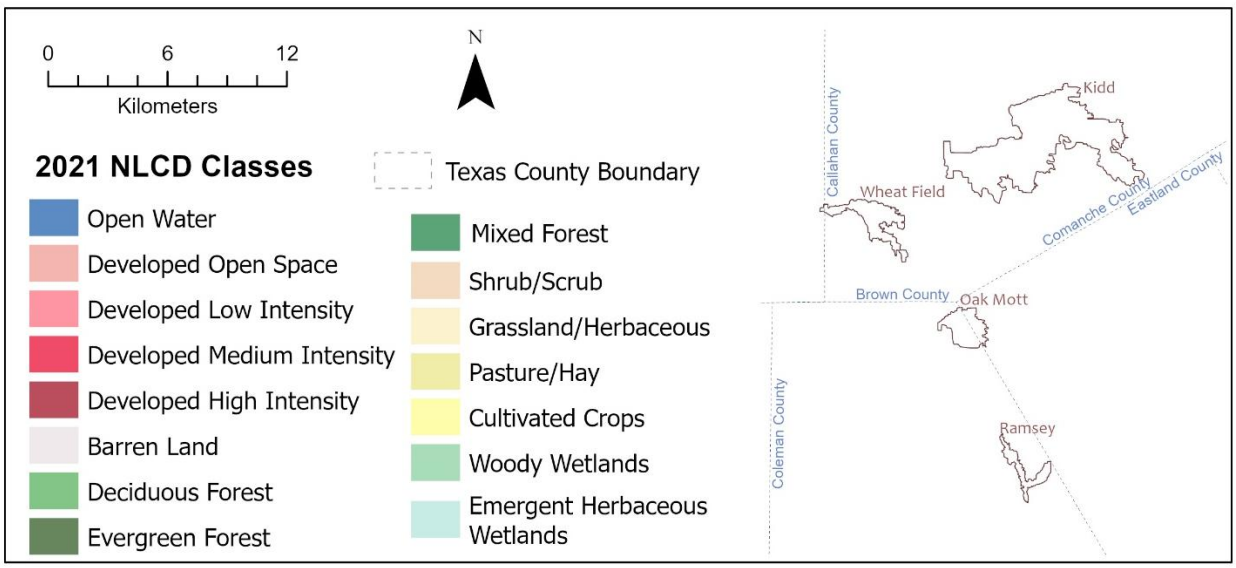


Figure 1: Study area with National Land Cover Database (NLCD) map overlay on Google Earth Engine and county perimeter

3. Data & Methods

The analysis focuses on the Eastland Complex Fire in north-central Texas, which burned during 16 March 2022 to 31 March 2022. The official fire perimeter from Texas A & M Forrest Service was used and modified to define the study area. All remote-sensing processing was constrained within this boundary. Two temporal windows were selected to characterize pre- and post-fire conditions: (i) a pre-fire window from 05-16 March 2022, and (ii) the earliest cloud-free post-fire period available in 01-11 April 2022 for optical indices.

Table 1: Datasets used in this study

Dataset	**Provider / Product**	**Variables**	**Spatial Resolution**	**Temporal Resolution and output**	**Purpose in Study**
Sentinel-1 SAR (IW, GRD)	ESA Copernicus	VV, VH backscatter; $\Delta\sigma^0$ (post-pre)	10 m	*Pre-fire range:* 05 Mar 2022 to 16 Mar 2022 *Post-fire range:* 01 Apr 2022 to 11 Apr 2022 (and 11 Apr 2023 for long-term moisture-loss)	Radar-based burn severity, backscatter loss, moisture-loss index, $\Delta\sigma^0$ classification
Sentinel-2 SR	ESA Copernicus	B8 (NIR), B12 (SWIR), QA60	10-20 m (NBR uses 20m SWIR)	Same as previous	Optical burn severity: NBR, dNBR, RdNBR; Validation of radar products
NBR / dNBR / RdNBR	Derived from Sentinel-2	NBR, dNBR, RdNBR	20 m	Pre- and post-fire composites	Burn severity reference; comparison with $\Delta\sigma^0$
Copernicus DEM GLO30	ESA	Elevation, Slope	30 m	Static dataset	Topographic characterization; slope-burn interactions
NLCD 2019 / 2021 Land Cover	USGS	Landcover Class (LC)	30 m	2021	Vegetation-type analysis; stratified $\Delta\sigma^0$-dNBR correlations
Random Sample Points	Derived from stacked rasters	$\Delta\sigma^0$, dNBR, RdNBR, slope, land cover	30 m sampling grid	Extracted from all raster after masking	Statistical correlation analysis (Python)
Moisture-Loss Index ($\Delta\sigma^0_{VV}+\Delta\sigma^0_{VH}$)	Derived from Sentinel-1	Combined VV+VH loss	10 m	Same as Sentinel-1 post-fire windows	Soil/vegetation moisture-loss inference. All datasets used in this study, with their sources, spatial resolutions and reference dates, are listed in Table 1.

Figure 2 and Figure S3 in supplemental documents provide a better understanding of the methodological workflow.

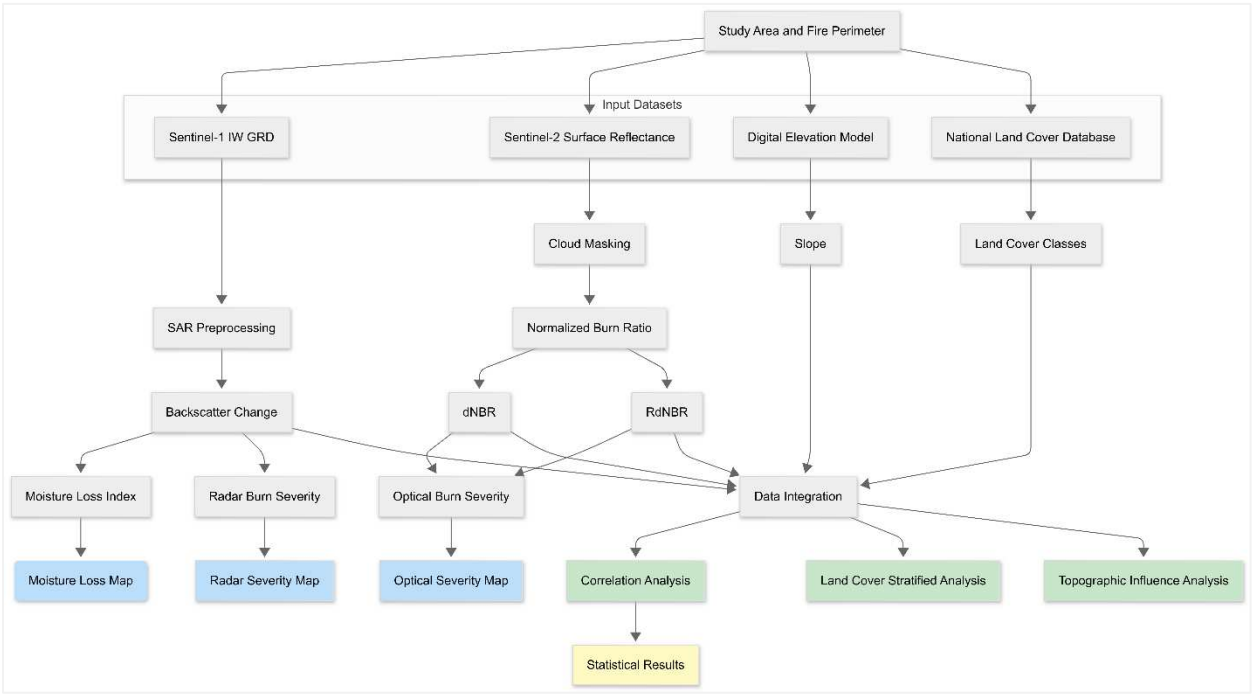


Figure 2: Methodological flowchart

3.1 Sentinel-1 SAR Processing

Sentinel-1 Interferometric Wide (IW) Ground Range Detected (GRD) scenes were collected for both VV and VH polarizations. Images were filtered by instrument mode (IW), product type (GRD), presence of the chosen polarizations and the defined pre- and post-fire date windows. Code can be accessed here: https://code.earthengine.google.com/?accept_repo=users/sonet/Eastland1 The COPERNICUS/S1_GRD collection used here is provided by Google Earth Engine already border-noise-removed, thermal-noise-removed, and radiometrically calibrated to sigma-nought; no additional terrain correction beyond the standard GRD product processing was applied prior to the speckle-filtering step described below.

3.1.1 Speckle filtering using a 3×3 Lee filter

Backscatter coefficients were first converted from decibels to linear power before applying a 3×3 Lee filter. This specific kernel size was selected to maximize speckle reduction while maintaining the sharp edges of the fragmented burn patches and agricultural boundaries characteristic of the Eastland landscape. While larger kernels (e.g., 5×5 or 7×7) were initially considered for their ability to further smooth homogeneous grasslands, they were ultimately rejected due to the risk of over-smoothing and losing the fine-scale structural detail of the unburned refugia identified within the fire perimeters.

3.1.2 Pre- and post-fire composites and $\Delta\sigma^0$ calculation

Filtered scenes were averaged to create pre-fire and post-fire mean composites for each polarization. Radar backscatter change was then computed as:

$$\Delta\sigma^0 = \sigma^0_{\text{post}} - \sigma^0_{\text{pre}}$$

Both $\Delta\sigma^0$(VV) and $\Delta\sigma^0$(VH) were derived. A combined moisture-loss metric was also generated by summing VV and VH changes and multiplying by −1 so that larger positive values reflected greater post-fire moisture and biomass loss. All radar products were exported for subsequent GIS and statistical analysis.

3.2 Sentinel-2 Optical Burn-Severity Indices

3.2.1 Cloud-masking and NBR calculation

Sentinel-2 Surface Reflectance images were used to compute optical burn indices. Cloud and cirrus contamination were removed using QA60 bitmasks. The QA60 bitmask is a metadata band included in Sentinel-2 imagery that provides quality assurance information at a 60-meter spatial resolution, specifically used to identify and filter out atmospheric obstructions. It operates by flagging specific bits within the data Bit 10 for opaque clouds and bit 11 for cirrus clouds allowing analysts to create binary masks that exclude these contaminated pixels from analysis. For each cloud-free image, the Normalized Burn Ratio (NBR) was computed as:

$$\text{NBR} = \frac{B8 - B12}{B8 + B12}$$

3.2.2 Multi-day composites and burn indices

Median pre-fire and post-fire NBR composites were generated to minimize noise from single-date variability. Median compositing was employed to generate spatially contiguous pre- and post-fire baselines. This statistical approach mitigates artifacts caused by cloud cover, shadows, and atmospheric opacity, while smoothing short-term phenological variations that could otherwise introduce bias into the burn severity assessment. Burn severity was quantified using both the difference NBR (dNBR) and relativized NBR (RdNBR). While dNBR calculates the absolute magnitude of change in vegetation health, its values are heavily influenced by pre-fire biomass, often resulting in lower severity ratings for sparse vegetation types. (Miller & Thode, 2007). RdNBR accounts for this bias by normalizing the differenced value against the pre-fire baseline, essentially scaling the severity based on the initial vegetation density. This relativization allows for a more consistent and accurate comparison of burn severity across heterogeneous landscapes containing both dense forests and sparse shrublands:

$$\text{dNBR} = \text{NBR}_{\text{pre}} - \text{NBR}_{\text{post}}$$

Table 2: Burn severity level and their ranges (Miller & Thode 2007)

Burn Severity Level	**dNBR Range** (scaled by 10^3)	**dNBR Range** (not scaled)

Enhanced Regrowth, high (post-fire)	–500 to –251	–0.500 to –0.251
Enhanced Regrowth, low (post-fire)	–250 to –101	–0.250 to –0.101
Unburned	–100 to +99	–0.100 to +0.099
Low Severity	+100 to +269	+0.100 to +0.269
Moderate-low Severity	+270 to +439	+0.270 to +0.439
Moderate-high Severity	+440 to +659	+0.440 to +0.659
High Severity	+660 to +1300	+0.660 to +1.300

Both rasters were exported for comparison against the Sentinel-1 backscatter-change data, with optical severity levels assigned following Table 2 (Miller & Thode, 2007). RdNBR is mathematically defined as:

$$\text{RdNBR} = \frac{\text{dNBR}}{\sqrt{|\ \text{NBR}_{\text{pre}}\ | + \epsilon}}$$

Where $|\ \text{NBR}_{\text{pre}}\ |$ serves as a proxy for pre-fire biomass density. The square-root transformation in the denominator is applied to better fit field observations in sparsely vegetated areas, preventing the index from becoming unstable where pre-fire biomass is low. (Miller et al., 2009). Interpreting RdNBR requires understanding that it measures the proportion of vegetation lost rather than the absolute quantity of biomass consumed. Consequently, a high severity fire in a sparse shrubland can yield a similar RdNBR value to a high severity fire in a dense forest, as both represent a near-total loss of the available pre-fire vegetation. This makes RdNBR particularly robust for comparing severity across diverse land cover types within the same fire perimeter. For classification purposes, this study adopted the widely cited thresholds established by Miller and Thode (2007), which categorize severity, as summarised in Table 3, as Unchanged/Low (< 69), Low (69-315), Moderate (316-640), and High (≥641). These thresholds align with the standard 4-class system used by monitoring programs like MTBS to ensure consistency and comparability across studies.

Table 3: Relativized difference NBR Classification severity level

Severity Class	**RdNBR Range**	**Interpretation**
Unchanged/Low	< 0.069	Minimal change relative to pre-fire.
Low	0.069 - 0.315	Low severity relative to initial density.
Moderate	0.316 - 0.640	Moderate severity relative to initial density.
High	≥0.641	High severity relative to initial density.

Initial RdNBR calculations revealed data gaps in sparsely vegetated areas due to the application of a stringent pre-fire vegetation mask (NBR > 0.1). To ensure spatial continuity across the entire study area, including grassland and shrubland zones with naturally low pre-fire NBR values, this masking threshold was removed. The stability of the relative index was maintained by applying a small epsilon value (ε = 0.001) to the denominator in the RdNBR equation. This specific value follows the technical standards used by the Monitoring Trends in Burn Severity (MTBS) program. Its inclusion prevents division-by-zero errors and stabilizes the index in areas where pre-fire

vegetation is exceptionally sparse, ensuring that the resulting severity values remain mathematically consistent across the diverse land cover types of the study area without excluding valid low-biomass pixels.

3.3 Terrain and Land-Cover Drivers

To assess environmental controls on burn severity, topographic and land-cover variables were incorporated into a stratified analysis. Elevation and slope (in degrees) were derived from the Copernicus GLO30 Digital Elevation Model (30 m resolution) using standard terrain algorithms, providing a mosaicking-artifact-free topographic baseline. For land cover, all analyses use the National Land Cover Database (NLCD) 2021 release. The terrain and land-cover analysis in Section 4.6 was originally computed using the NLCD 2019 release and a later post-fire compositing window; it has been re-run using NLCD 2021 and the same date window as the rest of the study, and the earlier configuration is retained and reported as a sensitivity analysis (Table S3). Analysis focused on the dominant classes within the fire perimeter, deciduous forest (41), evergreen forest (42), shrub/scrub (52), and grassland/herbaceous (71), which, together with pasture/hay, cultivated crops, and woody or emergent herbaceous wetlands, make up most of the study area's agricultural and semi-natural landscape. A burn mask (dNBR > 0.05) was applied to isolate the fire footprint, and zonal statistics were computed to determine mean severity per land-cover class. A pixel-based regression analysis was performed between slope steepness and dNBR to test whether topography influenced fire severity in this event. For joint analyses such as correlation, all layers were clipped to the fire perimeter and resampled to 30 m.

3.4 Sample Extraction for Statistical Analysis

A multi-band stack consisting of $\Delta\sigma^0$, dNBR, RdNBR, slope and NLCD land-cover class was constructed. Because the $\Delta\sigma^0$ raster is clipped to the fire perimeters, and because a common validity mask was applied requiring simultaneous valid data in all input layers, the effective sampling domain corresponds to the burned perimeters of the four fires rather than to the full administrative study area. Within this domain, simple random sampling was applied using the Earth Engine Image.sample function at 30 m resolution, drawing 3,000 points (random seed 42) for the pixel-wide and burn-only correlation analyses and 5,000 points (random seeds 42 and 99) for the land-cover-stratified and terrain analyses. Sampling was spatially unstratified: points were drawn with uniform probability across all valid pixels, so the number of points falling within a given land-cover class is proportional to the area of that class inside the burned perimeters rather than being fixed by design. Stratification by land cover was therefore applied post hoc, at the analysis stage, by grouping the sampled points by NLCD class. The spatial distribution of the sample points is shown in Figure S1, and the number of sample points obtained for each land-cover class is reported in Table S1. Samples were exported to CSV and analysed using Python.

3.5 Burn-only Analysis and $\Delta\sigma^0$ Optical Correlation

A burn-specific mask was created to isolate meaningful fire-affected pixels. Pixels were retained only where dNBR > 0.1 and $\Delta\sigma^0 < 0$ dB, indicating spectral/thermal burn signal and radar backscatter loss. Correlations were computed using Pearson's r between: $\Delta\sigma^0$ - dNBR and $\Delta\sigma^0$ - RdNBR. Scatter plots were generated for visual inspection. This analysis quantified the strength and direction of radar optical agreement across the fire scar.

3.6 Land-Cover-Specific Sensitivity Assessment

To determine how vegetation structure influences radar sensitivity, the sampled points were grouped post hoc by NLCD class. Classes represented by at least 30 valid samples were retained for analysis; classes falling below this threshold were excluded, and the sample size of every class, including those excluded, is reported in Table S1. For each retained land-cover class, separate Pearson correlations were computed between $\Delta\sigma^0$ and both optical indices (dNBR and RdNBR), and the correlation coefficient, p-value and sample size are reported together. Scatter plots were produced for key classes such as evergreen forest (42), shrub/scrub (52), and grassland/herbaceous (71). This approach isolated the vegetation-specific relationships between radar backscatter change and burn severity. All radar, optical, terrain, and land-cover products were integrated in a geographic information system (GIS) environment for visualization. Burn-severity maps from $\Delta\sigma^0$, dNBR, RdNBR, and the moisture-loss index were produced and compared spatially. Additional overlays and difference maps were used to highlight areas of agreement and divergence between radar- and optical-derived indicators, and to evaluate whether topography or vegetation cover influenced observed burn patterns. The Moisture Loss Index (MLI) is defined as -1 times the summed VV and VH backscatter change because fire-driven structural and moisture loss typically produces a negative backscatter change (Section 4.1); multiplying by -1 converts this loss into a positive-valued index, so that larger MLI values correspond to greater combined backscatter loss, consistent with the sign convention used for the burn-severity indices above. MLI is a combined backscatter-loss composite rather than a calibrated soil-moisture retrieval; this distinction, and the absence of independent moisture validation, is noted explicitly in Section 5.5.

$$\text{MLI} = -1 \times (\Delta\sigma^0_{VV} + \Delta\sigma^0_{VH})$$

3.7 Comparison with an Independent Burn-Severity Product

An independent comparison was made against the Monitoring Trends in Burn Severity (MTBS) product, an interagency programme that maps burn severity for all large fires in the United States. The 2022 MTBS thematic severity mosaic (USFS/GTAC/MTBS/ annual burn severity mosaics/v1) was sampled at the same points used for correlation analyses. MTBS severity is reported on a five-level thematic scale; to permit comparison, dNBR and RdNBR classes were harmonised onto the same four-level ordinal scale (unburned-to-low, low, moderate, high) by merging the moderate-low and moderate-high dNBR classes of Table 2, and pixels labelled as increased greenness or falling in the non-processing mask were excluded. Agreement was quantified using confusion matrices with overall and within-one-class agreement, and the relationship between $\Delta\sigma^0$ and the ordinal MTBS severity level was assessed using Spearman's rank correlation, overall and by land-cover class.

4. Results

Geospatial and radar analysis of the 2022 Eastland Complex Fire revealed a highly fragmented burn pattern. Across the total fire perimeter of 62,195 acres, only 25,916 acres (~41.67%) were classified as burned, with significant unburned refugia remaining within the perimeters. The Ramsey fire was the most spatially continuous, with 52.52% of its footprint burned, while the Oak Mott fire exhibited the highest fragmentation with only 37.09% of the area classified as burned.

4.1 Backscatter Analysis (Sentinel-1)

The analysis of Sentinel-1 Synthetic Aperture Radar (SAR) data revealed complex backscatter changes ($\Delta\sigma^0$) across the burned landscape. The Vertical-Vertical (VV) polarization change ranged approximately from -16.30 dB to +11.82 dB, while the Vertical-Horizontal (VH) polarization change ranged from -14.50 dB to +21.25 dB. Negative $\Delta\sigma^0$ values generally represented backscatter loss, driven by the combustion-induced reduction in vegetation structure and moisture. Conversely, positive $\Delta\sigma^0$ values corresponded to soil exposure, ash-covered ground, and roughness enhancement, which increased surface backscatter.

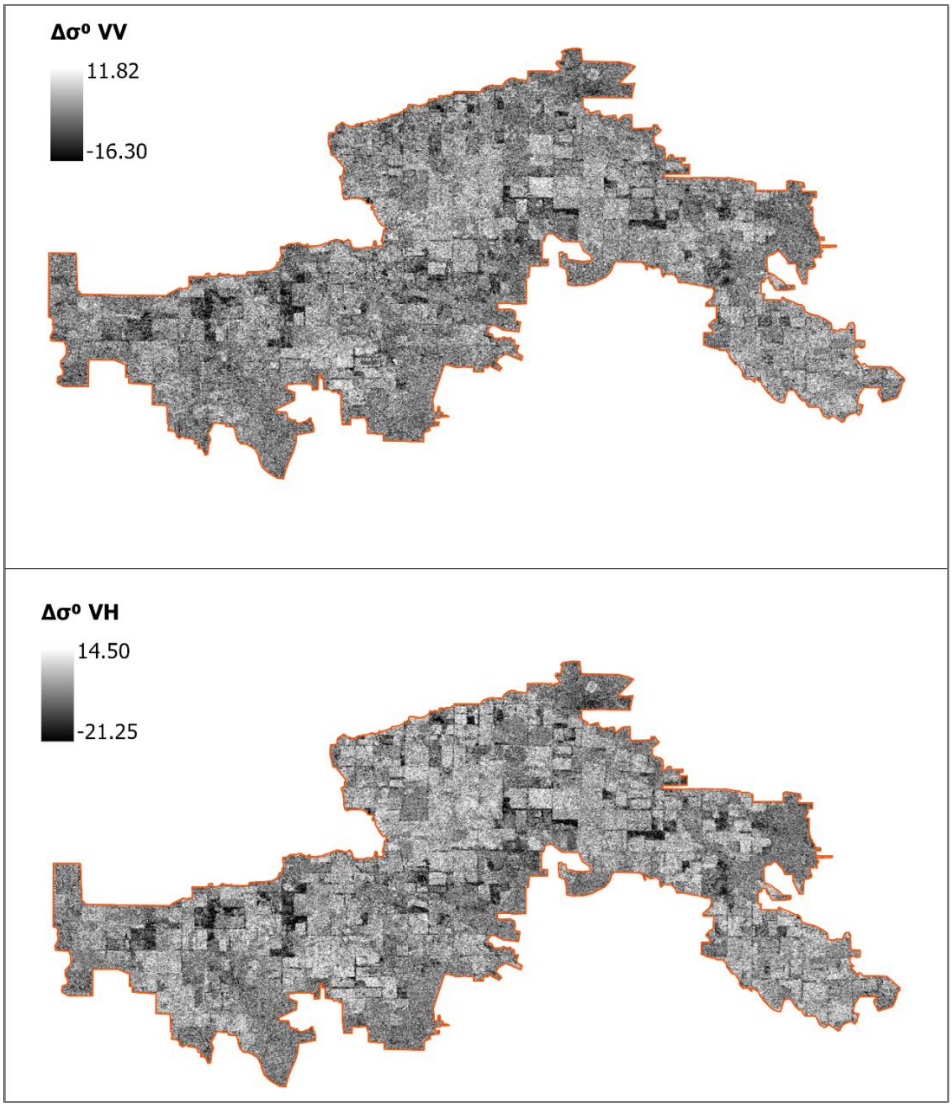


Figure 3: Radar backscatter change in the study area. Only Kidd fire is shown here for example. Next figure provides detailed understanding.

The quantitative analysis of the backscatter difference images revealed a notable disparity in the dynamic ranges of the two polarizations. The VH backscatter change signal exhibited a broader

range of variability (spanning 35.75 dB, from -21.25 to +14.50) compared to the VV backscatter change signal (spanning 28.12 dB, from -16.30 to +11.82).

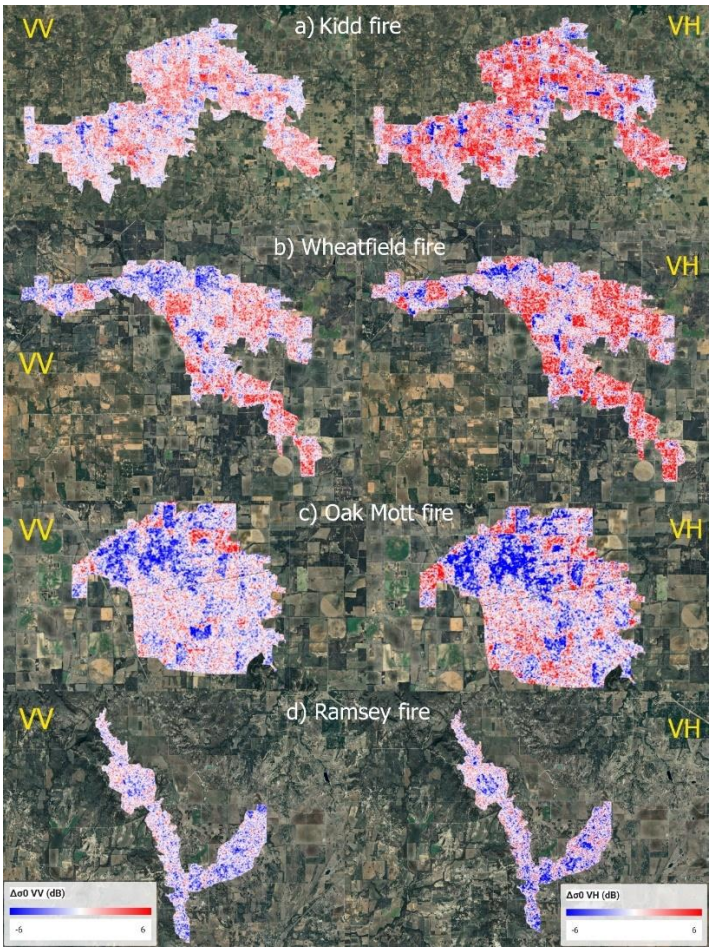


Figure 4: SAR Backscatter change spatial pattern. Backscatter values were speckle-filtered using a Lee-type adaptive filter in linear power space and differenced in decibel units, preserving the physical magnitude of change.

4.2 Burn Severity Assessment (Sentinel-2)

The optical burn-severity assessment, derived from Sentinel-2 data, utilized a four-level ordinal scale with values ranging from 0 to 3. Areas mapped as high-intensity burn (class 2-3) aligned spatially with the known severe fire fragments within the complex, specifically the Kidd, Oak Mott, Ramsey and Wheat Field fires. To ensure the reliability of these spectral indices, date ranges were selected to create stable pre-fire and post-fire image composites rather than relying on single-date acquisitions. This multi-day window approach reduced noise associated with temporary atmospheric anomalies, soil moisture fluctuations, and incidental rainfall. Consequently, the change signal (ΔNBR) represented a comparison between stable representative pre-fire and post-fire conditions, offering a more physically meaningful metric of disturbance (Hermosilla et al., 2024).

Figure 5 demonstrates the resulting Differenced Normalized Burn Ratio (dNBR) raster exhibited values ranging from approximately -0.53 to +0.28. This range is consistent with moderate-resolution optical burn severity mapping in low-stature vegetation landscapes. According to LANDFIRE Existing Vegetation Height (EVH) and Existing Vegetation Type (EVT) data, the Eastland Complex burn area is dominated by shrublands typically less than 1-3 meters in height and seasonal agricultural fields, primarily wheat, rather than tall closed-canopy forests. These vegetation types naturally produce lower spectral burn-severity contrast compared to conifer or broadleaf forest systems, which explains the limited upper-range dNBR signal observed in this study. The relatively narrow positive dNBR values are likely attributable to the short temporal separation of approximately one month, meaning vegetation had not yet undergone full physiological decline, as well as the limited vertical biomass of shrub and wheat fuels which reduces spectral contrast after combustion. Furthermore, the exposure of soil and ash likely led to mixed-pixel spectral dilution within the 10–20-meter resolution bands of Sentinel-2.

The four fires shared a common severity signature. In every perimeter the majority of pixels were classified as unburned and the burned fraction was dominated by the low-severity class, with dNBR values across the complex ranging from approximately -0.53 to +0.66 (Figures 5 and 6). Ramsey, the smallest fire, contained the highest proportion of moderate-high severity (1.8% of its perimeter), while moderate-high severity was essentially absent from the other three. Enhanced-regrowth pixels were confined to a small number of agricultural patches. These are most plausibly winter wheat fields that escaped the fire and continued to green up between the pre- and post-fire acquisitions, producing a negative dNBR that the classification scheme reports as regrowth rather than genuine post-fire recovery.

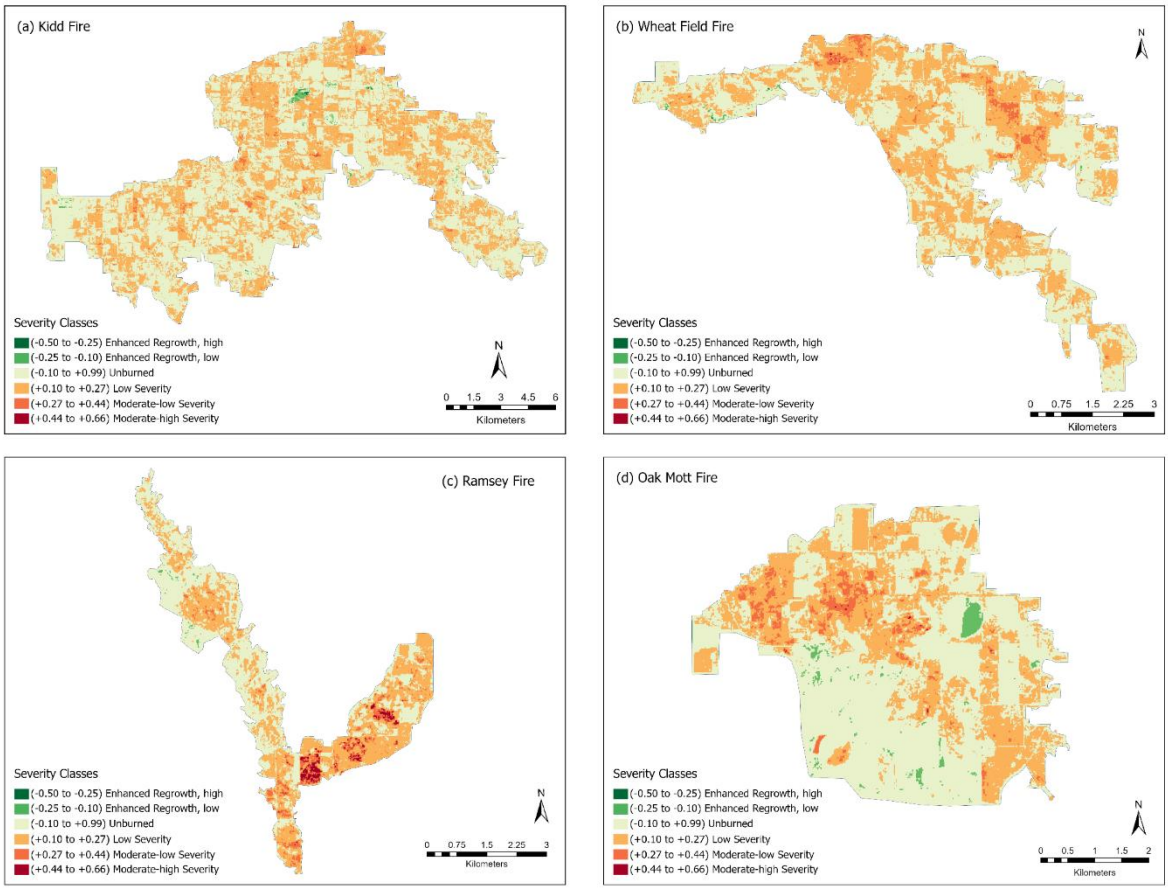


Figure 5: Sentinel-2 dNBR burn-severity classification for the four fires of the Eastland Complex: (a) Kidd, (b) Wheatfield, (c) Ramsey and (d) Oak Mott. Severity classes follow the dNBR ranges of Table 2. Panels are shown at individual scales; each carries its own scale bar.

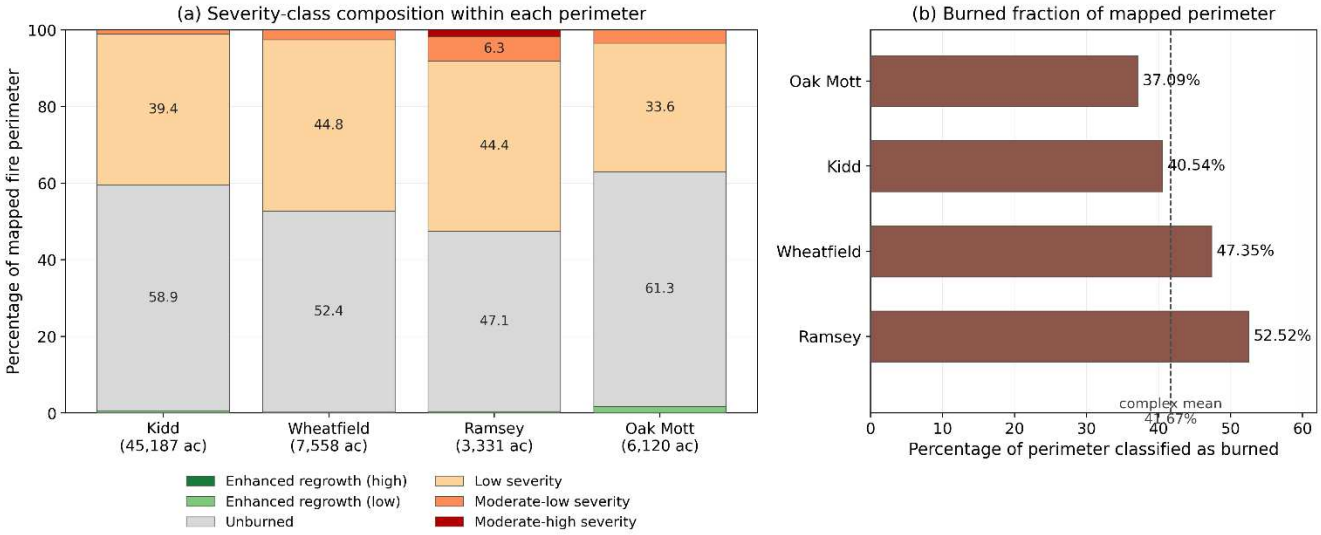


Figure 6: Quantitative comparison of burn severity among the four fires. (a) Severity-class composition as a percentage of each mapped perimeter; (b) percentage of each perimeter

classified as burned, that is, the sum of the low, moderate-low and moderate-high classes, with the complex-wide mean shown for reference. Areas are taken from Table 4.

Comparing the four fires quantitatively (Figure 6) shows that severity composition was broadly similar across the complex despite the ten-fold range in perimeter area. Unburned pixels dominate every perimeter, from 47.1% in Ramsey to 61.3% in Oak Mott, and the low-severity class accounts for most of the burned fraction in all four fires. Moderate-low severity remains below 3.6% everywhere except Ramsey (6.3%), and moderate-high severity is essentially absent outside Ramsey (1.8%), which is the smallest fire but the most severely burned by proportion. The burned fraction ranges from 37.09% (Oak Mott) to 52.52% (Ramsey) against a complex-wide mean of 41.67%. This quantitative comparison supports the interpretation of a fragmented, predominantly low-severity event and shows that the pattern is consistent across fires rather than driven by any single event.

One feature merits specific comment because it illustrates a non-fire process affecting both sensors. In the northern sector of the Oak Mott fire a distinct semicircular anomaly was observed within a centre-pivot irrigation field (Figure 4), with diverging optical and radar signatures: dNBR indicated low regrowth on one semicircle while the opposite semicircle showed a contrasting response in $\Delta\sigma^0VV$ and $\Delta\sigma^0VH$. This is attributable to asynchronous agricultural management rather than to fire, most likely differential tillage, harvesting or irrigation scheduling altering surface roughness and dielectric properties independently of the fire event.

Table 4: Summary of total affected fire perimeter accounted, and area burned shown in acres

Fire Events	**Enhanced Regrowth (high)**	**Enhanced Regrowth (low)**	**Unburned**	**Low Severity**	**Moderate-low Severity**	**Moderate-high Severity**	***Total burned area***
KiddFire	14.08	261.36	26593.2	17819.46	497.77	1.42	***40.54%***
OakMott	0.08	101.08	3748.64	2055.48	212.42	1.92	***37.09%***
Ramsey	0	11.72	1569.74	1477.75	210.19	61.36	***52.52%***
Wheatfield	0.5	16.68	3962.12	3385.77	191.41	1.17	***47.35%***
Total	**14.66**	**390.84**	**35873.70**	**24738.46**	**1111.79**	**65.87**	***41.67%***

Figures 5 and 6 and Table 4 reveal that the geospatial analysis of the burn severity distribution indicates that the Eastland Complex was characterized by a highly fragmented fire pattern, with the total burned area comprising only 41.67% of the mapped perimeters. Although reported burned area as 54,543 acres our analysis found total of 62,195 acres accounted as fire perimeter of which ~42% was burned on a ratio of total burned and unburned area. This suggests that despite the rapid spread, the fires left significant unburned refugia and agricultural tracts untouched within their boundaries. The Ramsey fire emerged as the most spatially continuous event, being the only fire where the burned area exceeded half of the total footprint (52.52%); this aligns with it also having the highest absolute area of moderate-high severity (61.36 acres), indicating a more intense and cohesive consumption of fuels. In contrast, the Oak Mott fire exhibited the lowest burned proportion (37.09%), reflecting a discontinuous burn scar likely broken by varying land use or fuel

gaps. The largest event, the Kidd fire, followed this patchy trend with only 40.54% of its area classified as burned, reinforcing the interpretation that these were primarily wind-driven, fast-moving fires that skipped over substantial portions of the landscape rather than consuming it entirely.

4.3 Multi-Sensor Correlation Analysis

This section evaluates the relationship between Sentinel-1 radar backscatter change ($\Delta\sigma^0$) and optical burn-severity indices using three progressively constrained analyses: (i) unfiltered pixel-wide correlations, (ii) burn-only correlations, and (iii) vegetation-stratified correlations. Both dNBR and RdNBR are examined separately to assess their relative suitability for low-biomass ecosystems.

4.3.1 $\Delta\sigma^0$ vs dNBR correlation across all pixels

Using all sampled pixels within the fire perimeters (n = 3,000; see Section 3.4), a weak, statistically significant negative correlation was observed between $\Delta\sigma^0$ (VV) and dNBR ($r = -0.252$, $p < 0.001$) due to presence of low severity burn with few regrowth and number of smaller areas burned. This indicates that, at the landscape scale, increasing optical burn severity is generally associated with a reduction in radar backscatter, consistent with the physical loss of vegetation volume and moisture.

However, the weak magnitude of the correlation ($|r| < 0.3$) suggests substantial scatter in the relationship. This is expected given that the dataset includes unburned and low-severity pixels, where natural variability in soil moisture, surface roughness, and land management practices can obscure fire-related radar signals. Thus, while the trend is statistically robust, it reflects a broad landscape response rather than a tightly coupled pixel-level relationship.

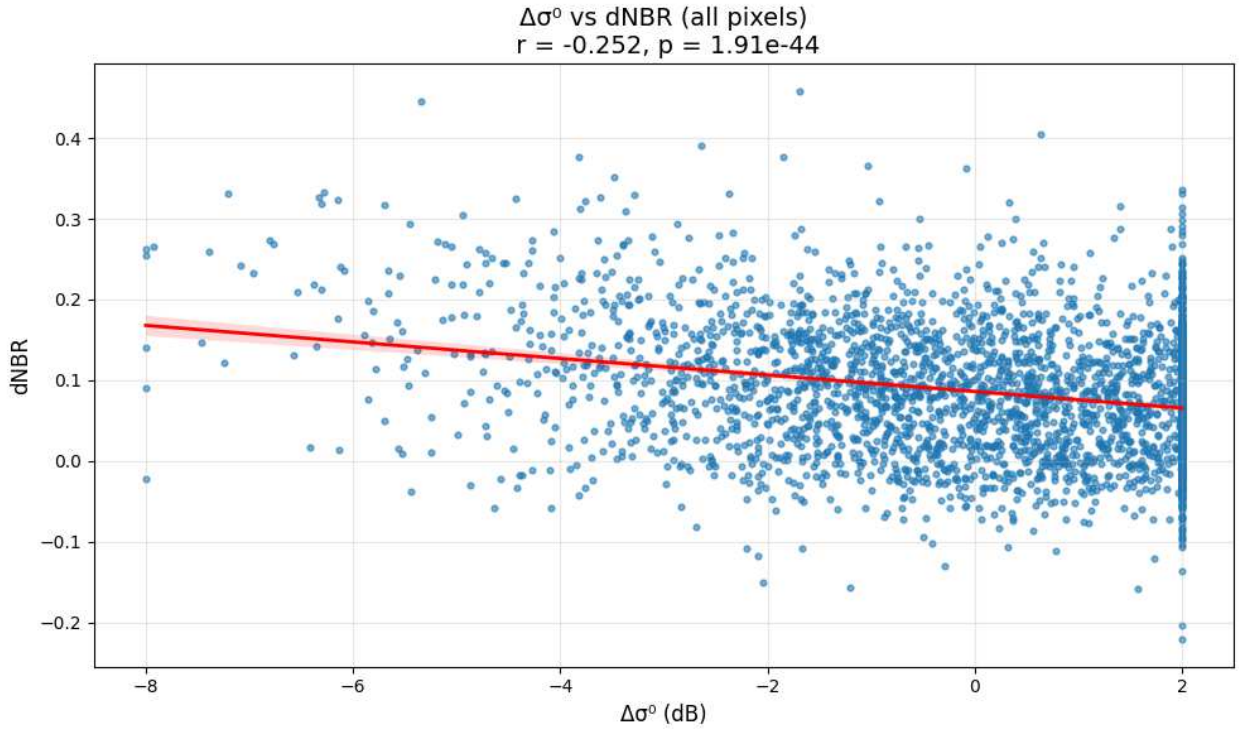


Figure 7: Δσ⁰ vs dNBR correlation across all pixels

4.3.2 Δσ⁰ vs dNBR correlation for burned pixels

To isolate fire-driven effects, the analysis was repeated using only burned pixels (dNBR > 0.1 and $\Delta\sigma^0 < 0$ dB). Under this constraint, the correlation strengthened slightly ($r = -0.296$, $p < 0.001$), confirming that the negative relationship between $\Delta\sigma^0$ and dNBR represents a genuine physical response to combustion rather than background noise.

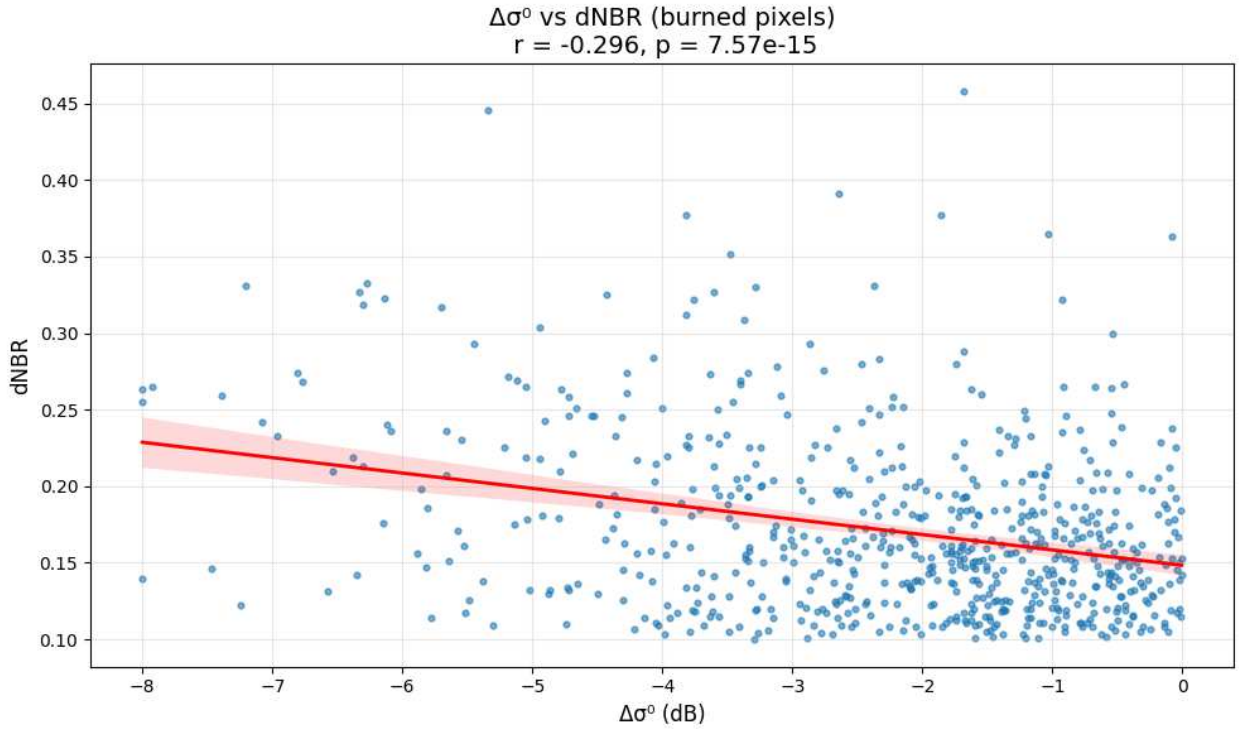


Figure 8: $\Delta\sigma^0$ vs dNBR correlation for burned pixels only

Despite the improvement, the correlation remains weak-to-moderate, indicating that optical burn severity and C-band radar backscatter are not tightly coupled in this landscape. This decoupling reflects the dominance of low-stature fuels (shrubs, grasses, and crops), where fire alters vegetation greenness more strongly than it alters physical structure detectable by C-band SAR. Unlike forested systems, the removal of fine fuels often produces insufficient changes in surface roughness or volume scattering to generate a strong linear radar response; the same pattern has been reported in Sentinel-1 burned-area mapping, where detection accuracy is highest over forest and lowest over grassland because pre- to post-fire backscatter variation is smaller in low-biomass cover types (Belenguer-Plomer et al., 2019).

4.3.3 $\Delta\sigma^0$ vs dNBR Correlation Stratified by Land Cover

When stratified by NLCD 2021 land-cover class, substantial variation emerged in the strength of $\Delta\sigma^0$-dNBR relationships. Forested classes exhibited the strongest correlations, with evergreen forest showing the strongest negative relationship of any class ($r = -0.533$, $p < 0.001$, $n = 552$), followed by deciduous forest ($r = -0.337$, $p = 0.004$, $n = 73$), reflecting the removal of vertically complex canopy structures detectable by both optical and radar sensors. Correlation coefficients, p-values and sample sizes for every land-cover class are reported in Table S1.

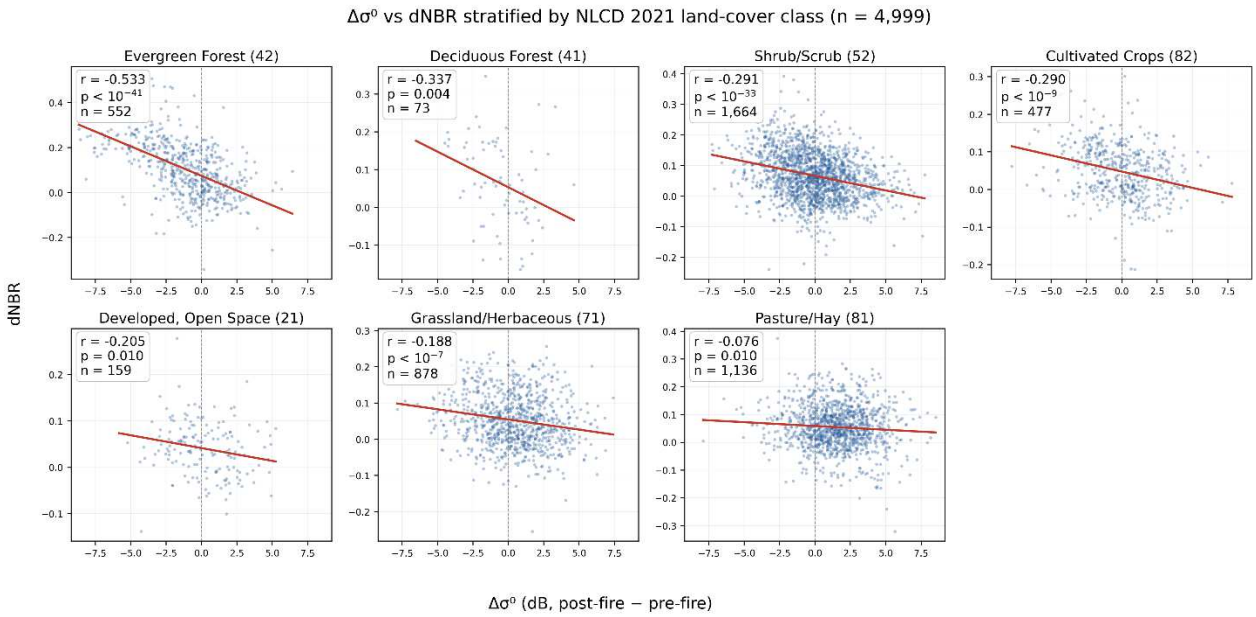


Figure 9: Δσ⁰ vs dNBR Correlation Stratified by Land Cover

Correlations within the dominant fuels of the region were weak. Shrub/scrub returned r = -0.291 ($p < 0.001$, n = 1,664) and grassland/herbaceous r = -0.188 ($p < 0.001$, n = 878). Although both are statistically significant, the significance is driven by sample size rather than effect size: $\Delta\sigma^0$ explains less than 10% of the variance in dNBR within either class. When the analysis was further restricted to burned pixels only (dNBR > 0.1 and $\Delta\sigma^0 < 0$ dB), these relationships weakened further and lost statistical significance entirely, falling to r = -0.087 ($p = 0.095$, n = 370) in shrub/scrub and r = -0.075 ($p = 0.451$, n = 103) in grassland/herbaceous, whereas evergreen forest retained a significant relationship under the same restriction (r = -0.279, $p < 0.001$, n = 227). This contrast quantifies a C-band sensitivity floor in low-biomass environments: the transition from standing grass or sparse shrubs to burned ground does not consistently produce a detectable change in radar backscatter. Among managed and anthropogenic classes, pasture/hay (r = -0.076, n = 1,136) and developed open space (r = -0.205, n = 159) exhibited the weakest relationships, while cultivated crops (r = -0.290, n = 477) was comparable to shrub/scrub; irrigation, tillage, and artificial surfaces plausibly introduce non-fire-related variability into the radar signal in these classes.

4.3.4 $\Delta\sigma^0$ vs RdNBR correlation across all pixels

Across all sampled pixels, the correlation between $\Delta\sigma^0$ and RdNBR was statistically significant but weak (r = -0.204, $p < 0.001$, n = 4,999), and consistently weaker than the corresponding $\Delta\sigma^0$-dNBR correlation over the same sample (r = -0.294). Per-class coefficients ranged from r = -0.392 in evergreen forest to r = -0.057 in pasture/hay, the latter not statistically significant (Table S1). Although dNBR and RdNBR are strongly correlated with one another across the sample (r = 0.71, $p < 0.001$), RdNBR consistently underperformed in its relationship with SAR backscatter. This underperformance reflects a structural limitation of RdNBR in semi-arid shrub and grass systems. RdNBR normalizes burn severity by pre-fire NBR, which is inherently low and spatially uniform in sparse vegetation. As a result, the normalization amplifies background noise rather than

enhancing true fire-induced signals, degrading its correspondence with radar-based structural change.

4.3.5 Δσ⁰ vs RdNBR correlation stratified by land cover

Vegetation-stratified analysis further confirmed the limited utility of RdNBR in this landscape. In shrub/scrub (NLCD 52) and grassland/herbaceous (NLCD 71) classes, Δσ⁰-RdNBR correlations were weak (r = -0.202 and r = -0.156, respectively), despite large sample sizes and high statistical significance driven by n rather than effect size. In developed open space and pasture/hay the RdNBR relationship was not statistically significant at all (r = -0.086, p = 0.279 and r = -0.057, p = 0.054, respectively). In every land-cover class examined, the Δσ⁰-RdNBR coefficient was weaker than the corresponding Δσ⁰-dNBR coefficient (Table S1).

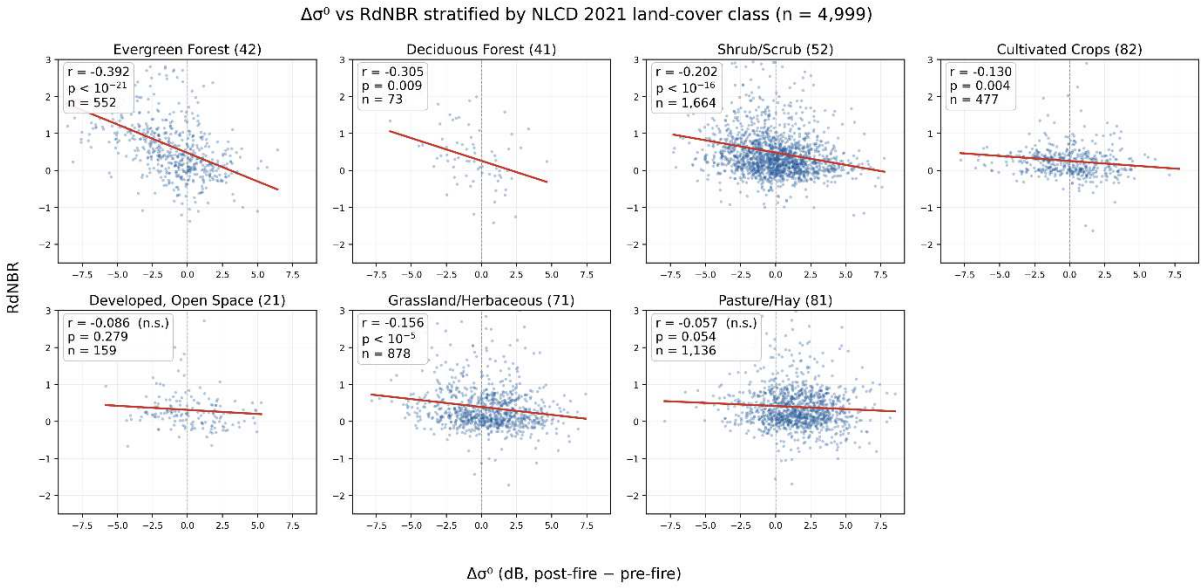


Figure 10: Δσ⁰ vs RdNBR correlation stratified by land cover

When analysis was restricted to moderate-to-high severity pixels within these classes, correlations were negligible and statistically insignificant. This reinforces the conclusion that RdNBR is poorly suited for multi-sensor integration in low-biomass systems, where pre-fire vegetation density is insufficient to support meaningful normalization.

4.3.6 Synthesis of dNBR vs RdNBR for SAR Integration

Taken together, these results demonstrate that dNBR is the more appropriate optical burn-severity metric for integration with Sentinel-1 SAR in the Eastland fire landscape. dNBR captures absolute reflectance changes associated with char, ash, and soil exposure that correspond more directly to radar-detected structural and moisture loss.

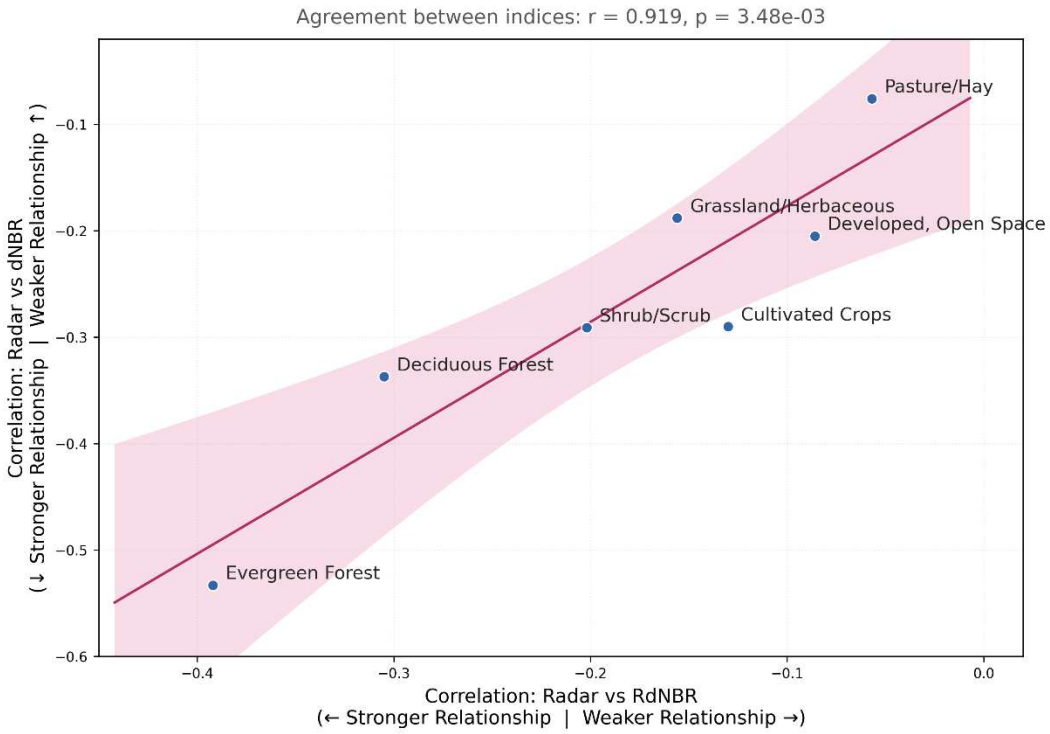


Figure 11: Correlation comparison across radar and optical analyzed data

The two optical indices rank the land-cover classes in a closely similar order: the per-class $\Delta\sigma^0$-dNBR and $\Delta\sigma^0$-RdNBR coefficients are themselves strongly correlated across the seven classes examined ($r = 0.919$, $p = 0.003$, $n = 7$ classes; Figure 11). This is a comparison between the two sets of class-level coefficients, and should not be confused with the pixel-level correlation between the indices themselves, which is weaker ($r = 0.71$; Section 4.3.4). Both optical indices correlate more strongly with radar ($\Delta\sigma^0$) in forested classes and lose that correlation in grassland and agricultural classes. The fire in these areas changed the vegetation's health/color (which dNBR saw) but did not significantly change the physical structure or biomass enough for the radar to detect it. Thus, RdNBR is better suited to high-biomass forested environments and introduces instability in shrub- and grass-dominated systems.

4.3.7 Statistical Robustness of the Reported Relationships

Because the correlations reported above are weak in absolute terms, we assessed their robustness rather than relying on significance testing alone; full results are given in Table S4 and Figure S2. Confidence intervals were obtained by bootstrap resampling (5,000 resamples), which is appropriate here because a Breusch-Pagan test indicates heteroscedastic residuals ($LM = 25.1$, $p < 0.001$) and a Jarque-Bera test rejects residual normality ($p < 0.001$), so parametric intervals would be optimistic. The pooled $\Delta\sigma^0$-dNBR coefficient is $r = -0.294$ with a 95% interval of [-0.319, -0.267], and the per-class intervals exclude zero for every class reported. Subsampling from 25% to 100% of the data returns coefficients between -0.293 and -0.296, so the estimates are not artefacts of sample size or of the random seed.

We also tested whether a linear coefficient is an adequate summary. Pearson and Spearman coefficients differ by no more than 0.037 in any class, indicating a close to monotonic-linear association. Adding a quadratic term to the pooled model raises the coefficient of determination from 0.086 to 0.101 and is statistically significant ($F = 82.0$, $p < 0.001$), but the additional 1.5 percentage points of explained variance shows the curvature is detectable at this sample size rather than substantial. In five-fold cross-validation, $\Delta\sigma^0$ alone predicts dNBR with an out-of-sample R^2 of 0.085, rising to 0.106 when land cover is included. A random-forest model fitted to $\Delta\sigma^0$, slope, elevation and land cover reaches a cross-validated R^2 of 0.164, against 0.109 for the equivalent linear model, indicating that some interaction structure is present that a single correlation coefficient does not capture. In that model $\Delta\sigma^0$ is the most important predictor of dNBR by permutation importance. Taken together these tests support the central claim of this study, which is that the radar-optical relationship is real but weak in this eco-region, and they place explicit bounds on how much of the variance in optical burn severity radar backscatter change can be expected to explain.

4.4 Comparison with an Independent Burn-Severity Product (MTBS)

To assess the optical and radar metrics against a reference produced independently of this study, all sample points were compared with the MTBS thematic burn-severity product for 2022 (n = 4,405 after harmonisation). The distribution of MTBS severity across the fire complex is itself informative: 89.3% of mapped pixels were assigned to the low severity class, 8.5% to unburned-to-low and 2.0% to moderate, with no pixel anywhere in the complex classified as high severity. MTBS therefore characterises the Eastland Complex as an extensive but predominantly low-severity event, which is consistent with the fine-fuel, wind-driven fire behaviour described in Section 4.2.

Agreement between the Sentinel-2 optical indices and MTBS differed markedly between the two indices. dNBR matched the MTBS class exactly for 37.8% of pixels but fell within one severity class of MTBS for 99.9% of them, with the disagreement almost entirely systematic: dNBR assigns a severity one class lower than MTBS, reflecting the fixed thresholds of Table 2 against the analyst-adjusted, per-fire thresholds MTBS applies. RdNBR agreed exactly for 29.9% of pixels but fell within one class for only 72.7%, with 27.3% of pixels assigned a severity two or more classes away from the MTBS value. This provides independent support for the conclusion of Section 4.3.6 that RdNBR behaves unstably in this landscape. Overall kappa values are low for both indices (0.07-0.09) because the strongly unbalanced MTBS class distribution inflates expected chance agreement, and the agreement percentages should be read together with that distribution.

The comparison of radar backscatter change against MTBS is the only genuinely cross-sensor test available here, and its outcome is strongly conditioned by land cover (Figure 12; Table S2). Across all classes combined the relationship is negligible ($\rho = -0.055$), but this global figure is misleading because it averages a real signal in woody vegetation with its absence elsewhere. In evergreen forest, $\Delta\sigma^0$ correlates with MTBS severity in the expected direction and with high significance ($\rho = -0.315$, $p < 0.001$, $n = 488$). In every other land-cover class the relationship is statistically indistinguishable from zero or negligible in magnitude: shrub/scrub ($\rho = -0.077$), grassland/herbaceous ($\rho = -0.004$), pasture/hay ($\rho = +0.055$) and cultivated crops ($\rho = +0.082$). By contrast, dNBR correlates significantly with MTBS in all seven classes examined ($\rho = +0.185$ to $+0.559$). Because MTBS is generated by a separate programme from Landsat imagery and an

independent processing chain, this pattern constitutes external corroboration of the C-band sensitivity floor identified in Section 4.3.3: C-band backscatter change tracks burn severity where vertically structured woody biomass is present, and loses that capability in the low-stature fuels that dominate this eco-region. It should be noted that MTBS assigns almost all of the complex to a single severity class, so the reference itself provides limited dynamic range against which to detect a severity gradient; the forest result is therefore best read as a positive finding rather than the absence of one being read as disproof elsewhere.

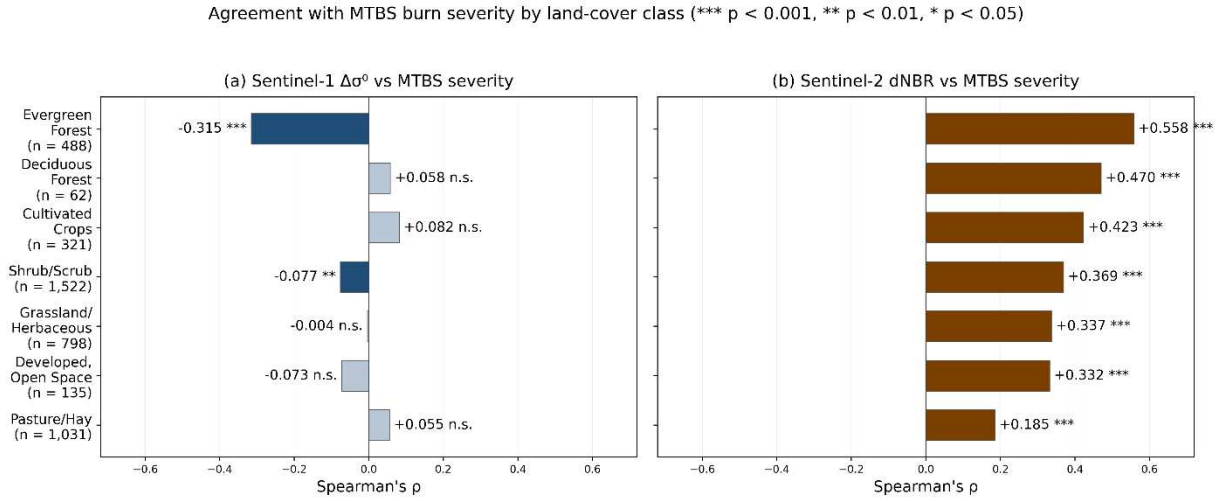


Figure 12: Agreement with MTBS burn severity by land-cover class. (a) Spearman's rank correlation between Sentinel-1 $\Delta\sigma^0$ and MTBS ordinal severity; (b) the same for Sentinel-2 dNBR. Solid bars denote statistically significant relationships ($p < 0.05$). $\Delta\sigma^0$ is significantly related to MTBS severity only in evergreen forest, whereas dNBR is significantly related in every class examined.

4.5 Moisture loss index

The SAR-derived Moisture Loss Index ranged from 0 to 12.59. High MLI values aligned spatially with confirmed burned polygons, successfully capturing hydrological deficits and dielectric changes that were undetectable by optical sensors due to smoke or rapid herbaceous recovery.

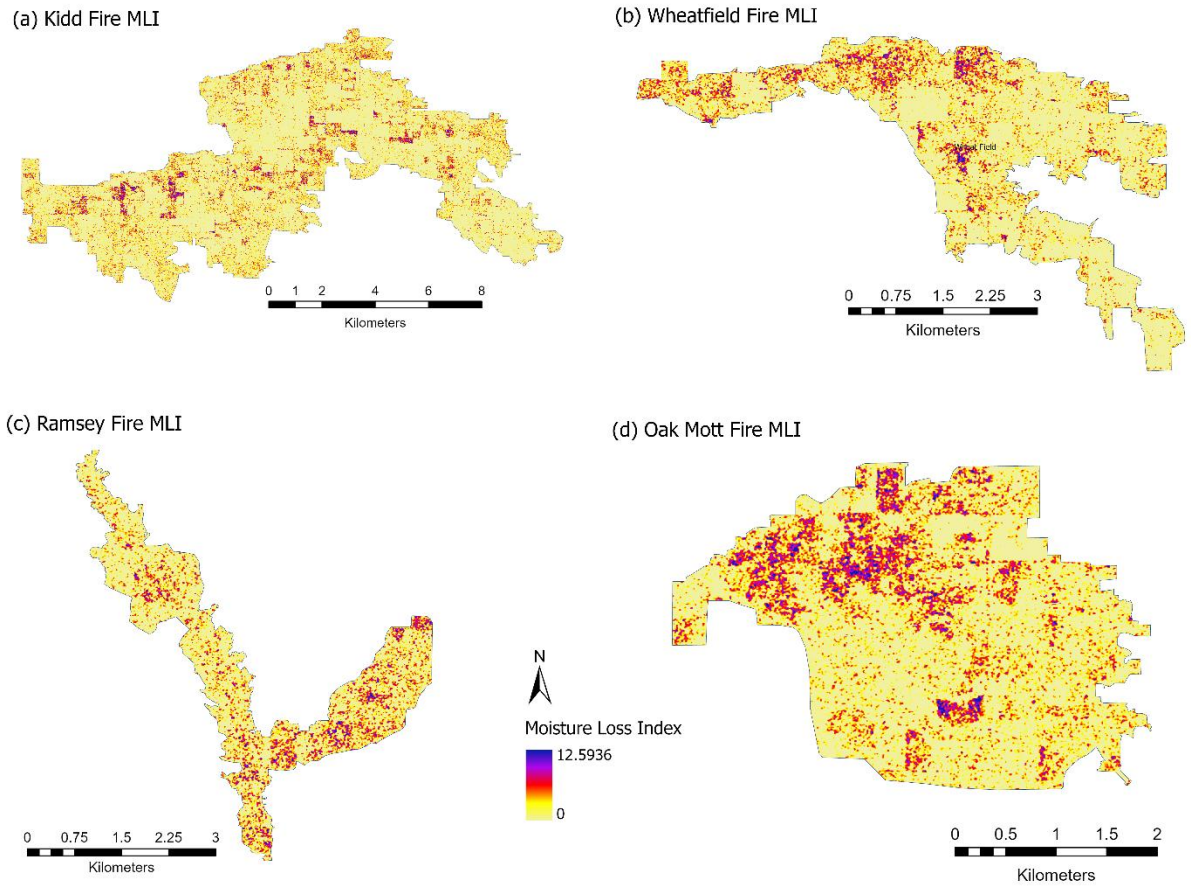


Figure 13: Moisture Loss Index (MLI) map, legend has been scaled to highest MLI for visualization

The MLI values should be interpreted relatively (spatial ranking) rather than as biophysical moisture percentages. The maps clearly represent that the burned areas have more moisture loss than unburned areas. Finally, consistent with the stronger radar-to-dNBR correlations observed in forested classes relative to shrub and grassland classes (Section 4.3.3) and the spatial agreement between MLI and dNBR patterns shown in Figure 17 (Section 5.1), Sentinel-1 backscatter change detection captured fire impacts across shrub and agricultural fuel environments even where optical dNBR exhibited limited dynamic range. SAR effectively detects combustion impacts under conditions where optical methods may be limited by vegetation type, background soil reflectance or atmospheric interference. The $\Delta\sigma^0$-dNBR relationship is inherently weaker in low-height shrub and wheat-field fuels, where volumetric scattering is minimal compared to taller closed-canopy forests. Post-fire microwave response is often immediate, whereas optical canopy or greenness response may lag, especially in semi-arid or winter agricultural settings. The moisture-loss index demonstrates added value of SAR for structural and dielectric change assessment, complementing optical spectral indices instead of replacing them.

4.6 Environmental Drivers of Severity

Elevation across the four fires spans 184 m (Figure 16), and less than 100 m within any individual fire; mean slope is 1.76 degrees with a maximum of 22.5 degrees. Within this narrow topographic range, burn severity showed a weak but statistically significant negative relationship with slope ($r = -0.053$, $p < 0.001$, $n = 4{,}767$) and a comparably weak positive relationship with elevation ($r = +0.051$, $p < 0.001$); slope accounts for less than 0.3% of the variance in dNBR. This supports the interpretation that the Eastland Complex was primarily a wind-driven event rather than a topography-driven one. The high-velocity winds during the event likely overwhelmed local topographic effects, driving the fire across flats and slopes with comparable intensity. Given the limited elevation range sampled here, this finding is specific to the Eastland study area and should not be generalized to transitional eco-regions with greater topographic relief.

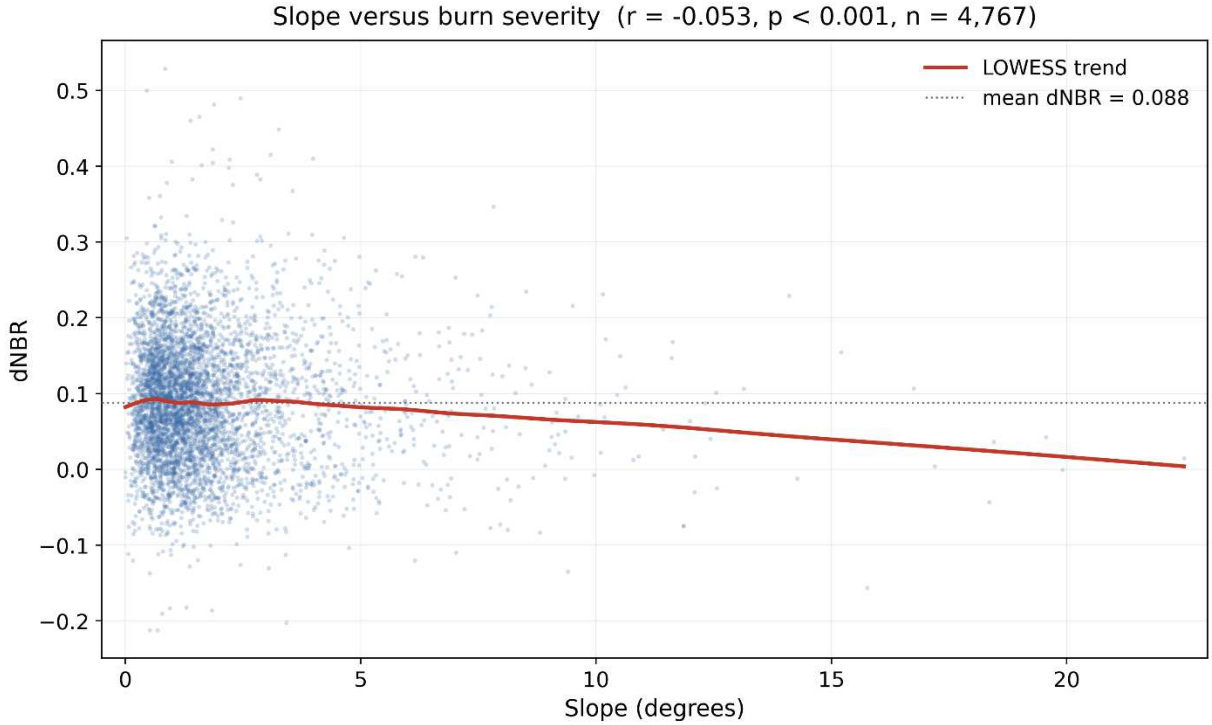


Figure 14: Locally weighted scatterplot smoothing (LOWESS) trend of slope versus dNBR

The LOWESS-smoothed relationship (Figure 14) shows dNBR remaining nearly constant below approximately 5 degrees, where the large majority of pixels lie, with a shallow decline at steeper slopes that rests on comparatively few observations; variability at any given slope greatly exceeds the fitted trend. In contrast, burn severity differed significantly among pre-fire land-cover classes (one-way ANOVA, $F(6, 4711) = 21.7$, $p < 0.001$). Evergreen and deciduous forest recorded the highest mean dNBR (0.118 for both), followed by pasture/hay (0.091), shrub/scrub (0.089) and grassland/herbaceous (0.079), with the lowest values in developed open space (0.070) and cultivated crops (0.067).

Because the terrain and land-cover analysis was originally computed over a later post-fire window (15 April - 10 May 2022) than the remainder of this study (1 - 11 April 2022), both configurations

were re-run and compared (Table S3). The later window yields a mean dNBR of -0.018 across the sample, that is, a net increase in vegetation greenness relative to pre-fire conditions, because herbaceous regrowth in this eco-region is rapid enough to remove much of the optical burn signal within six to eight weeks of the fire. Under that configuration slope shows no relationship with severity at all ($r = +0.001$, $p = 0.96$), and the land-cover ordering inverts, with cultivated crops recording the only positive mean dNBR of any class. The results reported above therefore use the 1 - 11 April window and the NLCD 2021 release throughout, consistent with Sections 4.1 to 4.4. This contrast is itself informative: in low-biomass transitional systems, the choice of post-fire compositing window over a span of only a few weeks determines whether an optical severity signal remains detectable at all, and reporting that window precisely is therefore essential.

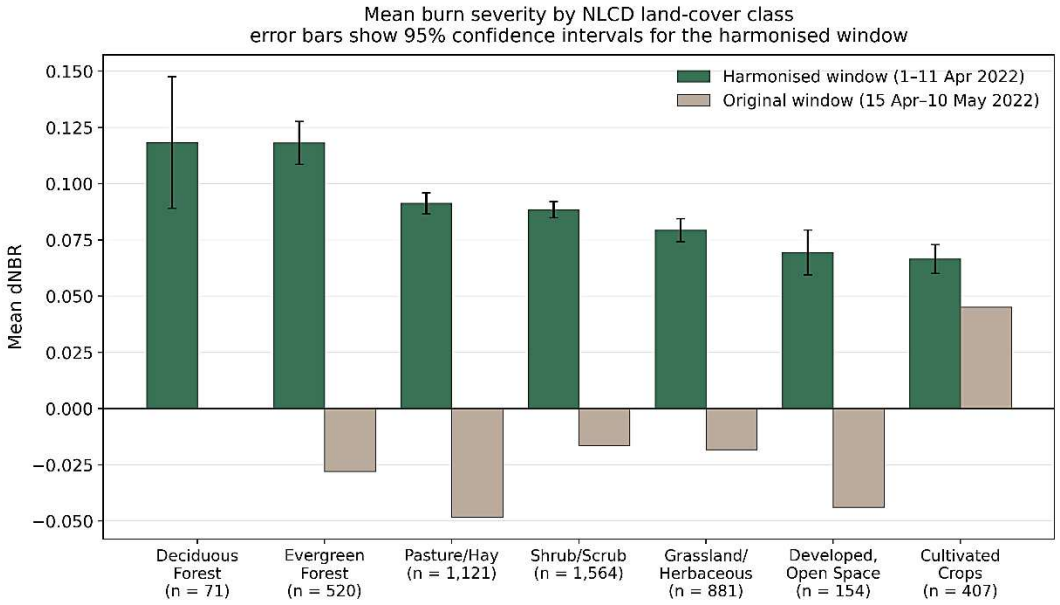


Figure 15: Mean-dNBR by NLCD class for only burned pixels

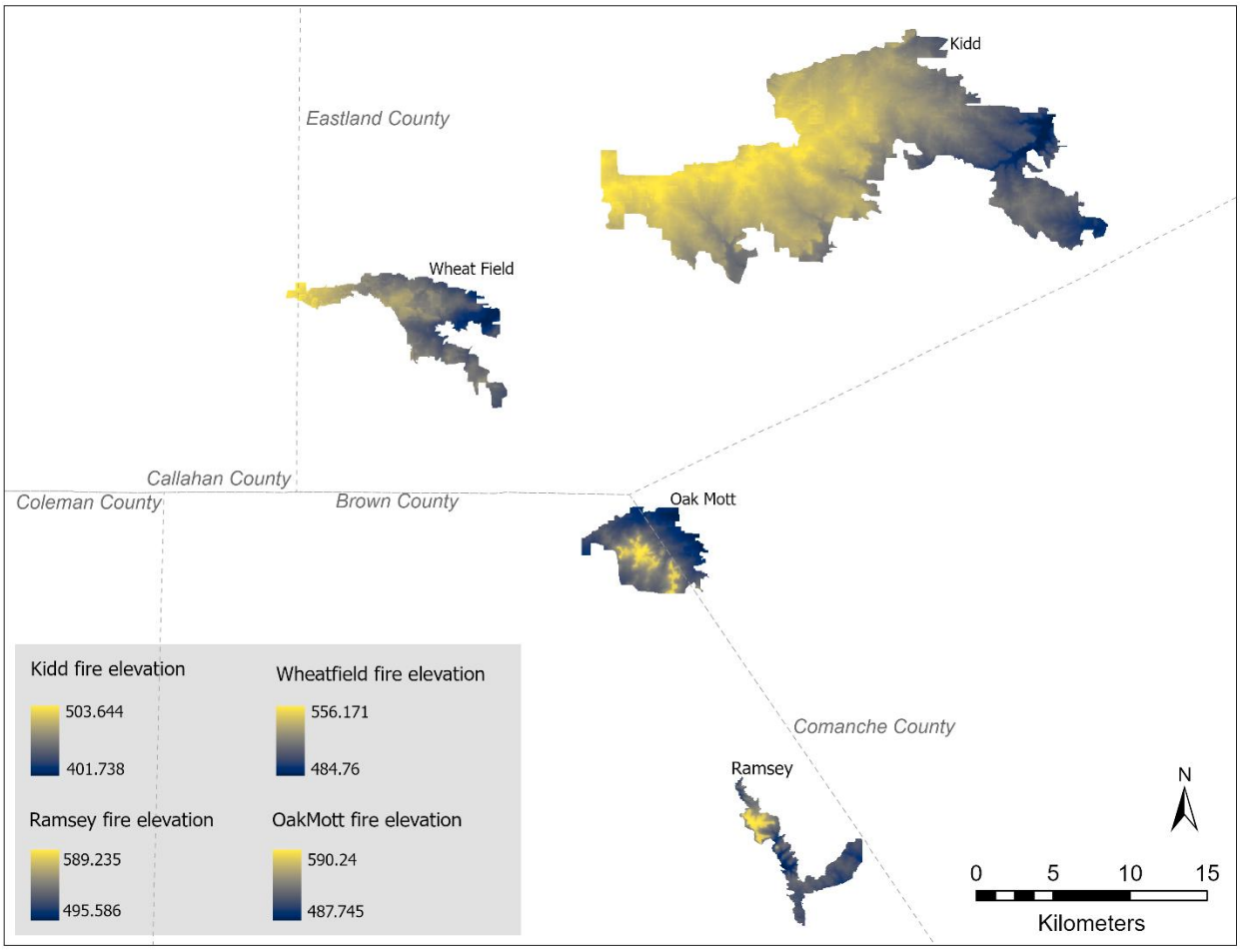


Figure 16: Elevation difference in the study area

Shrub/scrub areas exhibited significantly higher mean dNBR than grassland/herbaceous (difference 0.009, Welch t-test $p = 0.005$), consistent with the woody encroachment hypothesis of escalating fire risk in the Southern Great Plains, in which mesquite and juniper encroachment raises the potential for higher-severity fire effects relative to native grass prairie. However, shrub/scrub did not differ significantly from pasture/hay (difference -0.003, $p = 0.36$), so the present data support a distinction between shrub-encroached rangeland and open grassland but not between shrub-encroached rangeland and managed pasture. Taken together, these results indicate that fuel type rather than topographic control was the primary driver of spatial variability in burn severity for the Eastland fire.

5. Discussion

5.1 Radar and Optical Response to Fire in a Transitional Eco-region

The fuel types in this area (shrublands and grasslands) created a continuous fuel bed that allowed the fire to spread efficiently. This resulted in a cohesive burn scar with relatively few unburned patches inside the perimeter compared to a complex forest fire, leaving fewer spots for healthy green vegetation to appear in the final map. The results highlight the challenges of applying standard optical burn severity indices in the Southern Great Plains. The compressed dynamic range

of dNBR and the presence of negative values in clearly burned areas validate findings by Picotte et al. (2020), they noted that standard MTBS protocols often underestimate severity in non-forest biomes. In the Eastland Complex, the rapid post-fire response of herbaceous vegetation or green-up likely masked the severity of the burn in optical imagery acquired even a few weeks post-fire.

The observation that $\Delta\sigma^0$VH displayed a greater magnitude of change than $\Delta\sigma^0$VV that highlights the specific structural sensitivity of C-band radar in shrub-dominated ecosystems. This study demonstrates that Sentinel-1 SAR offers a viable proxy for burn severity. The observed increase in VV backscatter in many burned areas contradicts the standard "fire = backscatter loss" model often applied to dense forests (Tanase et al., 2010). In the open canopies of the Eastland region, fire acts as a "clearing agent," removing the attenuation of the grass/shrub layer and exposing the rougher, more reflective soil surface to the radar beam (Tanase et al., 2010). This aligns with recent findings by Millard et al. (2022) regarding C-band sensitivity to surface scattering. The bidirectional signal (loss in thickets, gain in grasslands) necessitates a context-aware interpretation of SAR data.

This bidirectional response can be explained mechanistically: the extreme decrease in VH values reflects near-total elimination of volume scattering, since pre-fire shrub canopies and standing grass depolarize the radar signal, and fire-driven removal of this biomass drives the cross-polarized return toward the sensor noise floor (Imperatore et al., 2017). Where positive VH values occur, one possible contribution is depolarization by charred, skeletal woody debris; we note this as a candidate mechanism only, since the present GRD data do not permit the polarimetric decomposition that would be required to test it. Because VV responds mainly to the comparatively stable ground surface while VH is sensitive to the full vegetation volume (Imperatore et al., 2017) undergoing this soft-to-charred transformation, VV shows a narrower dynamic range than VH across the burn scar.

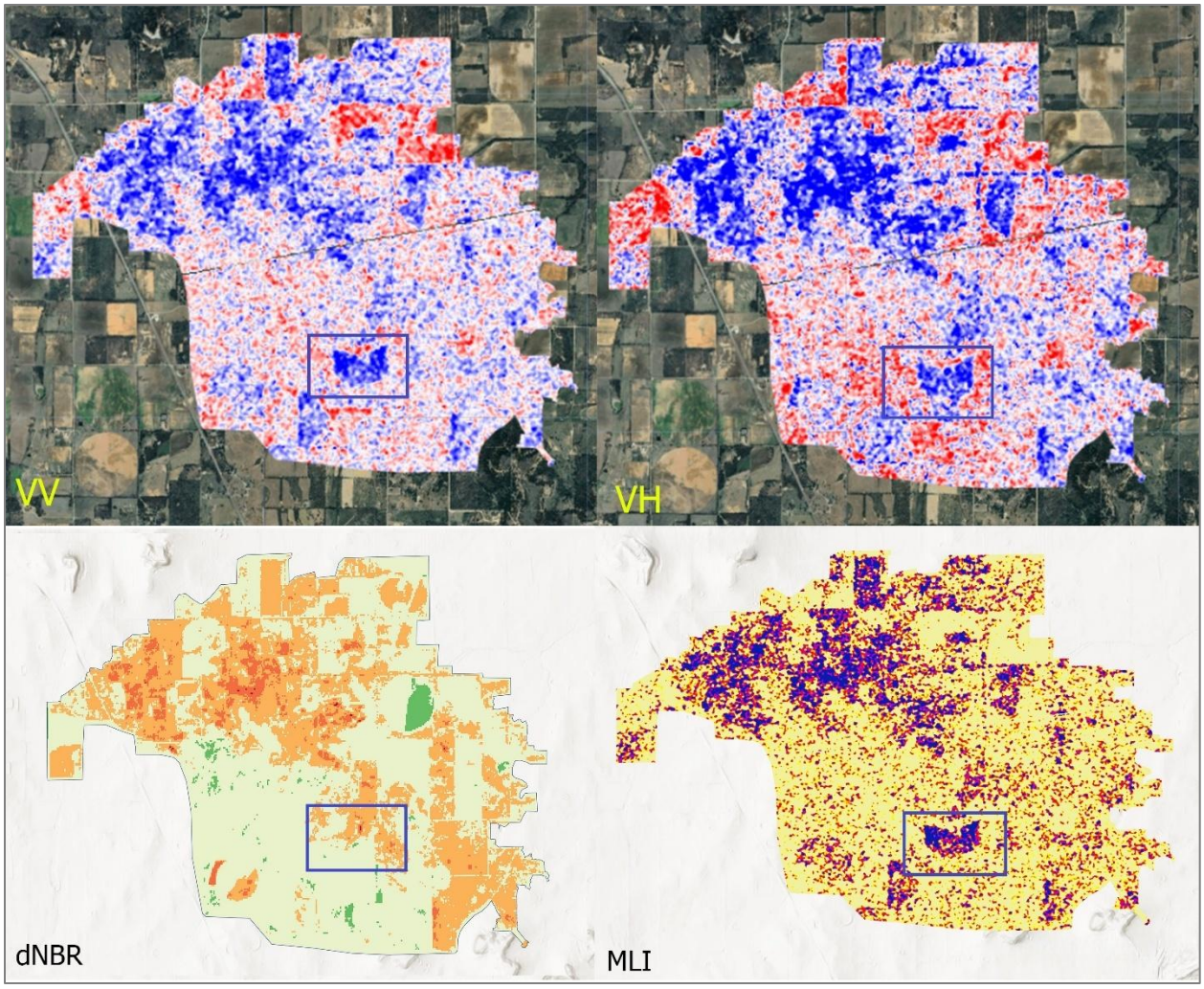


Figure 17: Comparative analysis among spatially mapped radar derived backscatter change data, moisture loss index and sentinel-2 derived burn severity map

In figure 17 it can be seen that in Sentinel-1 backscatter change maps for $\Delta\sigma^0_{VV}$, $\Delta\sigma^0_{VH}$ and the moisture loss index map, the marked areas showed identical shape but dNBR map did not detect that rather it show unburned-low severity-moderate low severity burned areas. The co-occurrence of this feature across SAR-based metrics indicates that the affected area experienced measurable fire-induced changes in vegetation structure and moisture content. In contrast, the absence of a comparable signal in dNBR suggests limited sensitivity of optical greenness-based indices to these changes.

This discrepancy is attributable to fundamental differences in sensor response mechanisms. Sentinel-1 backscatter is sensitive to variations in dielectric properties, surface roughness, and canopy structure (Tanase et al., 2010; Imperatore et al., 2017), allowing it to capture sub-canopy damage, biomass loss, and post-fire drying even where spectral vegetation greenness changes are minimal. MLI, as an uncalibrated composite of VV and VH backscatter loss, is expected to respond to the combined structural and dielectric changes that follow fire, although it was not validated against independent moisture measurements in this study (Section 5.5). By comparison, dNBR

primarily responds to changes in canopy chlorophyll and reflectance in the near-infrared and shortwave infrared bands and therefore may fail to detect fire impacts in areas characterized by low pre-fire biomass, sparse vegetation, or rapid post-fire recovery.

The observed divergence highlights a known limitation of optical burn-severity indices in grassland-shrubland and agriculturally dominated landscapes, where fire may substantially alter vegetation structure and moisture without producing strong spectral greenness contrasts. These findings demonstrate that SAR-derived backscatter change and moisture-based metrics provide complementary and, in some cases, more sensitive indicators of fire effects than dNBR alone. Integrating SAR and optical observations is therefore critical for accurately characterizing burn severity and fire impacts across heterogeneous and low-biomass environments.

5.2 Environmental Controls on Burn Severity

The minimal influence of slope coupled with the significant influence of land cover paints a clear picture of the Eastland Complex as a fuel- and weather-driven disaster. The significantly higher severity in Shrub/Scrub zones points to the role of mesquite and juniper encroachment in altering the fire regime. These woody fuels burn hotter and longer than the native grasses, leading to more severe ecological impacts. From a socio-environmental perspective, this reinforces the need for fuel management strategies that target woody encroachment, particularly in the Wildland-Urban Interface (WUI) where these fuels about human infrastructure (Katuwal & Kafley, 2024).

In this study, dNBR showed a substantially stronger relationship with $\Delta\sigma^0_{VV}$ than RdNBR, indicating that dNBR is the more appropriate optical burn-severity metric for the Eastland fire landscape. This result is consistent with the dominant fuel types in the area's low-stature shrubs (1-3 m), grasses, and sparse herbaceous cover. In such systems, pre-fire NBR values are already low and spatially uniform because the vegetation has limited canopy moisture and weak near-infrared contrast. RdNBR normalizes burn severity by the magnitude of pre-fire NBR, which is designed for forests where dense canopies and highly variable biomass create strong pre-fire NBR gradients. In shrub-grass ecosystems, however, the normalization step amplifies noise and suppresses true burn-severity signals, causing RdNBR to lose sensitivity. This explains the near-zero $\Delta\sigma^0$-RdNBR correlations across NLCD 52 and 71.

Besides, dNBR responds directly to post-fire reflectance changes related to char, ash, and exposed soil, which remain detectable even in sparse fuels. As a result, $\Delta\sigma^0$ and dNBR exhibit a much stronger and statistically significant coupling, with $\Delta\sigma^0$ effectively capturing the same structural and moisture losses that drive dNBR increases. Consequently, dNBR provides a more reliable burn-severity indicator for semi-arid shrub and grass systems like Eastland, whereas RdNBR is better suited to high-biomass forested environments. Given the minimal elevation range in the Eastland fire area, topographic effects on C-band backscatter are negligible; therefore, vegetation-driven patterns were prioritized.

The minimal influence of slope compared to land cover confirms that the Eastland Complex was a fuel-driven disaster exacerbated by decades of land management decisions. From a policy standpoint, the high sensitivity of the VH channel to woody biomass loss provides a quantifiable metric for the efficacy of prescribed burns and brush-clearing initiatives aimed at protecting the

expanding WUI. By integrating these active sensing capabilities, state agencies can move beyond reactive suppression and toward a proactive, data-driven framework for regional fire resilience. These conclusions regarding dNBR/RdNBR performance and woody-encroachment effects on severity are drawn from a single fire complex in a low-relief, low-biomass transitional eco-region and should be tested across additional fires and regions before being generalized more broadly.

Two aspects of these environmental results were not anticipated and merit comment. First, terrain slope correlates more strongly with $\Delta\sigma^0$ ($r = -0.153$, $p < 0.001$) than with dNBR ($r = -0.053$), despite the negligible influence of topography on burn severity itself in this low-relief landscape. Because terrain cannot plausibly affect the radar signal through fire behaviour here, the most likely explanation is a residual local-incidence-angle effect in the backscatter data, incidence angle being among the acquisition parameters known to control C-band response alongside surface geometry and dielectric properties (Imperatore et al., 2017). This is a measurement artefact rather than an ecological signal, and it reinforces the need for terrain-corrected backscatter in low-relief settings where the fire signal itself is weak. Second, although shrub/scrub burned at significantly higher mean dNBR than grassland/herbaceous, consistent with the woody encroachment hypothesis, it did not differ significantly from pasture/hay. The expectation that shrub-encroached rangeland would separate cleanly from all herbaceous cover types is therefore only partly supported, and managed pasture appears to carry fuel loads comparable to encroached rangeland in this eco-region.

5.3 Index Behaviour and Operational Relevance

The moisture-loss index's all-weather capability may offer near-term value for provisional fire-extent assessment when optical imagery is obscured by cloud or smoke, complementing rather than replacing existing MTBS/Sentinel-2-based workflows. Realizing this potential operationally would require the independent validation discussed in Section 5.5, which has not yet been performed.

The observed decoupling between $\Delta\sigma^0$ and RdNBR in shrubland and grassland classes, with r values of -0.202 and -0.156 respectively, points to a fundamental mathematical instability in relativized indices within semi-arid transitional zones. While RdNBR is a recognized standard for temperate conifer forests, its performance degrades in landscapes where the pre-fire baseline, NBRpre, is naturally low. In the Texas Cross Timbers, the sparse canopy and high background soil reflectance result in NBRpre values that often approach the limit of detection. When these values are used in the denominator of the RdNBR equation, small variations in spectral reflectance driven by soil moisture or sensor noise rather than fire effects are disproportionately amplified. These findings suggest that for the Southern Great Plains, absolute change represented by dNBR provides a more physically accurate representation of fire-induced biophysical alteration, as it avoids the numerical sensitivity inherent in the relativization of low-biomass pixels.

The cross-polarized VH channel responds to the loss of three-dimensional woody structure, which is of practical relevance in the Southern Great Plains where mesquite (Prosopis glandulosa) and juniper (Juniperus spp.) encroachment has been associated with shifts in fire regime. Because the VH signal tracks woody biomass loss while dNBR is dominated by the rapid greening of herbaceous fuels, radar-derived structural metrics may remain informative after the grass layer has recovered. We note, however, that the present data distinguish shrub/scrub from open grassland

but not from managed pasture (Section 4.6), so this application requires testing against independent measures of woody cover before it could be relied upon operationally.

These index results are consistent with the design assumptions of the indices themselves and with previous evaluations. RdNBR was introduced to compensate for variation in pre-fire vegetation condition by normalising dNBR against the pre-fire NBR (Miller & Thode, 2007), and subsequent calibration work established its performance in forested systems where that denominator is large and stable (Miller et al., 2009). Its weaker performance here is therefore a predictable consequence of applying it where the pre-fire baseline is small, rather than a contradiction of earlier work; Soverel et al. (2010) likewise reported that the relative merits of dNBR and RdNBR depend on the vegetation context in which they are applied. The land-cover gradient we observe also reproduces a pattern reported independently for Sentinel-1 burned-area mapping, in which detection accuracy was highest over forest and lowest over grassland because pre- to post-fire backscatter variation is smaller in low-biomass cover types (Belenguer-Plomer et al., 2019). That our comparison against MTBS recovers the same ordering, in a different eco-region and using severity agreement rather than detection accuracy, suggests that the constraint is a property of C-band sensing in sparse fuels rather than of any particular algorithm.

A critical advantage of the integrated SAR-optical framework demonstrated here is its temporal robustness. Wildfires in Texas often coincide with frontal passages and subsequent atmospheric instability, leading to prolonged cloud cover that blinds sensors like Sentinel-2. Furthermore, the rapid recovery of fine fuels can lead to a quick spectral return to baseline conditions, where dNBR values may decrease within weeks of the event. Because Sentinel-1 C-band SAR is an active system capable of penetrating smoke and clouds, it provides an immediate assessment capability. The moisture-loss index developed in this study captures the post-fire hydrological deficit, offering emergency managers a reliable map of fire extent and initial severity even before the first clear multispectral window becomes available.

5.4 Fire Fragmentation and Unburned Refugia

The finding that only 41.67% of the total perimeter area was classified as burned highlights the highly fragmented nature of the Eastland Complex. These unburned areas within the perimeter are ecologically vital, serving as seed sources for native vegetation recovery and habitat islands for displaced fauna. The ability of the moisture-loss index to clearly delineate these unburned fragments, even when dNBR showed low-severity ambiguity, demonstrates the superior spatial precision of microwave remote sensing in characterizing fire heterogeneity. Understanding this fragmentation is essential for post-fire resilience monitoring, as it indicates a mosaic-style burn that may recover more rapidly than a contiguous high-severity landscape.

This fragmentation estimate should be read with the threshold convention in mind, since the burned fraction is defined by the dNBR class boundaries of Key and Benson (2006) and would shift if different boundaries were adopted. The independent MTBS mapping supports the broader characterisation: it assigns 89.3% of the complex to the low severity class and no pixel anywhere to high severity, describing the same event as extensive but predominantly low in severity.

5.5 Limitations and Future Work

While this study successfully utilized Google Earth Engine-native GRD data, the lack of phase information (InSAR) limited the ability to quantify precise soil moisture deficits at depth. Future research should leverage offline processing of SLC data to generate interferometric coherence and closure phase maps, which offer higher sensitivity to soil moisture anomalies. Additionally, the lack of contemporaneous field plots (Composite Burn Index) means the radar-optical relationships reported here remain uncalibrated against any absolute severity scale. Future research prioritising field data collection in these transitional biomes would allow absolute radar severity scales to be established. This study also has several additional limitations. The optical and radar metrics were compared against the independent MTBS thematic severity product (Section 4.4), but no field-based reference data such as Composite Burn Index plots were available, and none can now be collected for a fire that burned in March 2022 in a rapidly recovering herbaceous system. MTBS is itself derived from Landsat dNBR, so the optical comparison is a consistency check rather than a fully independent validation, and because MTBS assigns 89.3% of the complex to a single severity class it offers limited power to validate severity gradients. Confounding factors affecting Sentinel-1 backscatter, including soil-moisture variability, agricultural practices such as tillage and irrigation, crop phenology, and incidence-angle effects, were not independently controlled for and may influence observed changes in managed land-cover classes. The statistical analysis relies solely on Pearson correlation, which does not capture nonlinear relationships or provide uncertainty quantification; cross-validation, regression diagnostics, and machine-learning comparisons were not performed. Conclusions regarding RdNBR performance and the influence of woody encroachment on burn severity are drawn from a single wildfire event in a low-relief study area and require confirmation across additional fires and regions before broader generalization. Finally, the terrain and land-cover analysis in Section 4.6 originally used a later post-fire compositing window and the NLCD 2019 release; both have now been brought into line with the rest of the study, and the earlier configuration is retained and reported as a sensitivity analysis in Table S3.

A further limitation concerns comparison with earlier C-band work. Much of the published evidence on SAR burn severity comes from closed-canopy forest, including the Mediterranean pine systems in which C-band backscatter was found to increase with severity (Tanase et al., 2010), whereas the dominant response here is backscatter loss in a sparse, predominantly herbaceous landscape. Differences between our results and that literature therefore reflect contrasting biomes and fire regimes as much as differences in method, and direct numerical comparison across those studies should be treated with caution.

Conclusion

This study compared Sentinel-1 SAR backscatter change with Sentinel-2 optical burn-severity indices (dNBR, RdNBR) for the 2022 Eastland Complex Fire, a transitional eco-region where optical indices are known to underestimate severity due to rapid vegetation recovery and low pre-fire biomass. Sentinel-1 backscatter, particularly the cross-polarized VH channel, proved more sensitive to structural loss than optical greenness in this low-biomass setting, and dNBR consistently outperformed RdNBR as the optical index best suited for integration with radar in this study area. Fuel type, especially woody encroachment by mesquite and juniper, was a stronger

driver of burn severity here than topography, which had minimal influence given the site's limited elevation range.

These findings, drawn from a single fire complex, should be confirmed across additional fires and regions before being generalized. Future work should prioritize independent field validation (e.g., Composite Burn Index or MTBS comparison) and Interferometric SAR (InSAR) phase information to calibrate absolute radar severity thresholds and quantify soil-moisture deficits more precisely.

Declaration of generative AI and AI-assisted technologies in the writing process

During the preparation of this manuscript, the author(s) used generative AI tools to assist with improving readability. After using these tools, the author(s) reviewed and edited the content as needed and take(s) full responsibility for the content of the published article.

Data availability

Data will be made available on request. Additionally, code can be accessed here: https://code.earthengine.google.com/?accept_repo=users/sonet/Eastland1 and high resolution maps can be accessed here: https://utdallas.box.com/s/beq2ffc67mey7ahvceddvz8d7apgaimp

References

Beloiu, M., Heinzmann, L., Rehush, N., Gessler, A., & Griess, V. C. (2023). Individual tree-crown detection and species identification in heterogeneous forests using aerial RGB imagery and deep learning. *Remote Sensing*, *15*(6), 1463. https://doi.org/10.3390/rs15051463

Brown, A. R., Petropoulos, G. P., & Ferentinos, K. P. (2018). Appraisal of the Sentinel-1 & 2 use in a large-scale wildfire assessment: A case study from Portugal's fires of 2017. *Applied Geography*, *100*, 78–89. https://doi.org/10.1016/j.apgeog.2018.10.004

Brown, E. K., Wang, J., Feng, Y., de Beurs, K. M., Henebry, G. M., & Hanes, J. M. (2021). US wildfire potential: A historical view and future projection using high-resolution climate data. *Environmental Research Letters*, *16*(3), 034060. https://doi.org/10.1088/1748-9326/aba868

Burnett, J. T., & Edgeley, C. M. (2023). Factors influencing flood risk mitigation after wildfire: Insights for individual and collective action after the 2010 Schultz Fire. *International Journal of Disaster Risk Reduction*, *94*, 103791. https://doi.org/10.1016/j.ijdrr.2023.103791

Cahoon, D. R., Stocks, B. J., Levine, J. S., Cofer, W. R., & Chung, C. C. (1992). Evaluation of a technique for satellite-derived area estimation of forest fires. *Journal of Geophysical Research: Atmospheres*, *97*(D4), 3805–3814. https://doi.org/10.1029/91JD03080

Cardil, A., Mola-Yudego, B., Blázquez-Casado, Á., & González-Olabarria, J. R. (2019). Fire and burn severity assessment: Calibration of Relative Differenced Normalized Burn Ratio (RdNBR) with field data. *Journal of Environmental Management*, *235*, 342–349. https://doi.org/10.1016/j.jenvman.2019.01.077

Chuvieco, E., & Congalton, R. G. (1989). Application of remote sensing and geographic information systems to forest fire hazard mapping. *Remote Sensing of Environment*, *29*(2), 147–159. https://doi.org/10.1016/0034-4257(89)90023-0

Donovan, V. M., Crandall, R., Fill, J., & Wonkka, C. L. (2023). Increasing large wildfire in the eastern United States. *Geophysical Research Letters*, *50*(21), e2023GL107051. https://doi.org/10.1029/2023GL107051

Giglio, L., Csiszar, I., & Justice, C. O. (2006). Global distribution and seasonality of active fires as observed with the Terra and Aqua Moderate Resolution Imaging Spectroradiometer (MODIS) sensors. *Journal of Geophysical Research: Biogeosciences*, *111*(G2), G02016. https://doi.org/10.1029/2005JG000142

Hermosilla, T., Wulder, M. A., White, J. C., & Coops, N. C. (2024). Clouds and image compositing. In J. A. Cardille, M. A. Crowley, D. Saah, & N. E. Clinton (Eds.), *Cloud-based remote sensing with Google Earth Engine* (pp. 235–252). Springer. https://doi.org/10.1007/978-3-031-26588-4_15

Hitchcock, H. C., & Hoffa, R. M. (1974). Mapping a recent forest fire with ERTS-1 MSS data. In F. Shahrokhi (Ed.), *Remote sensing of earth resources* (Vol. 3, pp. 449–461). University of Tennessee.

Holden, Z. A., & Jolly, W. M. (2011). Modeling topographic influences on fuel moisture and fire danger in complex terrain to improve wildland fire management decision support. *Forest Ecology and Management*, *262*(12), 2133–2141. https://doi.org/10.1016/j.foreco.2011.08.002

Howe, A. A., Blomdahl, E. M., Smith-Eskridge, E., Pinto, D. R., Brunson, M. W., Howe, P. D., ... Klain, S. C. (2024). Worldviews more than experience predict Californians' support for wildfire risk

mitigation policies. *Environmental Research Letters*, *19*(5), 054025. https://doi.org/10.1088/1748-9326/ad3cf6

Hu, X., Zhang, P., & Ban, Y. (2023). Large-scale burn severity mapping in multispectral imagery using deep semantic segmentation models. *ISPRS Journal of Photogrammetry and Remote Sensing*, *196*, 228–240. https://doi.org/10.1016/j.isprsjprs.2022.12.015

Jaffe, D. A., O'Neill, S. M., Larkin, N. K., Holder, A. L., Peterson, D. L., Halofsky, J. E., & Rappold, A. G. (2020). Wildfire and prescribed burning impacts on air quality in the United States. *Journal of the Air & Waste Management Association*, *70*(6), 583–615. https://doi.org/10.1080/10962247.2020.1749731

Kane, V. R., Lutz, J. A., Roberts, S. L., Smith, D. F., McGaughey, R. J., Povak, N. A., & Brooks, M. L. (2013). Landscape-scale effects of fire severity on mixed-conifer and red fir forest structure in Yosemite National Park. *Forest Ecology and Management*, *287*, 17–31. https://doi.org/10.1016/j.foreco.2012.08.044

Katuwal, H., & Kafley, H. (2024). Playing with fire: Socioeconomic factors and deliberate wildfires in Texas. *Journal of Environmental Management*, *370*, 122980. https://doi.org/10.1016/j.jenvman.2024.122980

Key, C. H., & Benson, N. C. (2006). *Landscape assessment: Ground measure of severity, the Composite Burn Index; and remote sensing of severity, the Normalized Burn Ratio* (General Technical Report RMRS-GTR-164). U.S. Department of Agriculture, Forest Service, Rocky Mountain Research Station. https://doi.org/10.2737/RMRS-GTR-164

Langaas, S. (1992). Temporal and spatial distribution of savanna fires in Senegal and the Gambia, West Africa, 1989-90, derived from multi-temporal AVHRR night images. *International Journal of Wildland Fire*, *2*(1), 21–36. https://doi.org/10.1071/WF9920021

Lee, H. J., Shin, M. Y., & Kim, N. R. (2025). Droughts and PM2.5 air pollution in California: The roles of wildfires. *Environment International*, *202*, 109678. https://doi.org/10.1016/j.envint.2025.109678

Martin, M. G. F. (1993). The rational role of experience. *Proceedings of the Aristotelian Society*, *93*(1), 71–88. https://doi.org/10.1093/aristotelian/93.1.71

Martini, L., Faes, L., Picco, L., Iroumé, A., Lingua, E., Garbarino, M., & Cavalli, M. (2020). Assessing the effect of fire severity on sediment connectivity in central Chile. *Science of the Total Environment*, *728*, 139006. https://doi.org/10.1016/j.scitotenv.2020.139006

Mass, C., & Ovens, D. (2024). The meteorology of the August 2023 Maui wildfire. *Weather and Forecasting*, *39*(7), 1115–1134. https://doi.org/10.1175/WAF-D-23-0182.1

Matson, M., & Holben, B. (1987). Satellite detection of tropical burning in Brazil. *International Journal of Remote Sensing*, *8*(4), 509–516. https://doi.org/10.1080/01431168708948657

Millard, K., Darling, S., Pelletier, N., & Schultz, S. (2022). Seasonally-decomposed Sentinel-1 backscatter time-series are useful indicators of peatland wildfire vulnerability. *Remote Sensing of Environment*, *283*, 113329. https://doi.org/10.1016/j.rse.2022.113329

Miller, J. D., Knapp, E. E., Key, C. H., Skinner, C. N., Isbell, C. J., Creasy, R. M., & Sherlock, J. W. (2009). Calibration and validation of the relative differenced Normalized Burn Ratio (RdNBR) to three measures of fire severity in the Sierra Nevada and Klamath Mountains, California, USA. *Remote Sensing of Environment*, *113*(3), 645–656. https://doi.org/10.1016/j.rse.2008.11.009

Miller, J. D., & Thode, A. E. (2007). Quantifying burn severity in a heterogeneous landscape with a relative version of the delta Normalized Burn Ratio (dNBR). *Remote Sensing of Environment*, *109*(1), 66–80. https://doi.org/10.1016/j.rse.2006.12.006

Morresi, D., Marzano, R., Lingua, E., Motta, R., & Garbarino, M. (2022). Mapping burn severity in the western Italian Alps through phenologically coherent reflectance composites derived from Sentinel-2 imagery. *Remote Sensing of Environment*, *269*, 112800. https://doi.org/10.1016/j.rse.2021.112800

Novo, A., Regos, A., & Fernández, C. (2025). Machine learning-based predictions of soil burn severity using spectral and LiDAR remote sensing data. *Forest Ecology and Management*, *596*, 123094. https://doi.org/10.1016/j.foreco.2025.123094

Pereira, M. C., & Setzer, A. W. (1993). Spectral characteristics of deforestation fires in NOAA/AVHRR images. *International Journal of Remote Sensing*, *14*(3), 583–597. https://doi.org/10.1080/01431169308904358

Picotte, J. J., Bhattarai, K., Howard, D., Lecker, J., Epting, J., Quayle, B., Benson, N., & Nelson, K. (2020). Changes to the Monitoring Trends in Burn Severity program mapping production procedures and data products. *Fire Ecology*, *16*, Article 16. https://doi.org/10.1186/s42408-020-00076-y

Rahman, M. T., & Rashed, T. (2015). Urban tree damage estimation using airborne laser scanner data and geographic information systems: An example from 2007 Oklahoma ice storm. *Urban Forestry & Urban Greening*, *14*(3), 562–572. https://doi.org/10.1016/j.ufug.2015.05.003

Rahmati, M., Amelung, W., Brogi, C., Dari, J., Flammini, A., Bogena, H., ... Vereecken, H. (2024). Soil moisture memory: State-of-the-art and the way forward. *Reviews of Geophysics*, *62*(2), e2023RG000828. https://doi.org/10.1029/2023RG000828

Soverel, N. O., Perrakis, D. D. B., & Coops, N. C. (2010). Estimating burn severity from Landsat dNBR and RdNBR indices across western Canada. *Remote Sensing of Environment*, *114*(9), 1896–1909. https://doi.org/10.1016/j.rse.2010.03.013

Szpakowski, D. M., & Jensen, J. L. R. (2019). A review of the applications of remote sensing in fire ecology. *Remote Sensing*, *11*(23), 2742. https://doi.org/10.3390/rs11232742

Tanase, M. A., Santoro, M., de la Riva, J., Pérez-Cabello, F., & Le Toan, T. (2010). Sensitivity of X-, C-, and L-band SAR backscatter to burn severity in Mediterranean pine forests. IEEE Transactions on Geoscience and Remote Sensing, 48(10), 3663-3675. doi: 10.1109/TGRS.2010.2049653.

Imperatore, P., Azar, R., Calò, F., Stroppiana, D., Brivio, P. A., Lanari, R., & Pepe, A. (2017). Effect of the vegetation fire on backscattering: An investigation based on Sentinel-1 observations. IEEE Journal of Selected Topics in Applied Earth Observations and Remote Sensing, 10(10), 4478-4492. https://doi.org/10.1109/JSTARS.2017.2717039

Belenguer-Plomer, M. A., Tanase, M. A., Fernandez-Carrillo, A., & Chuvieco, E. (2019). Burned area detection and mapping using Sentinel-1 backscatter coefficient and thermal anomalies. Remote Sensing of Environment, 233, 111345. https://doi.org/10.1016/j.rse.2019.111345

Thomas, A. S., Schlickman, E. E., & Trujillo-Falcón, J. E. (2025). Before the flames: California WUI residents' understanding of fire weather warnings and personal preparation around wildfire.

International Journal of Disaster Risk Reduction, *120*, 105396. https://doi.org/10.1016/j.ijdrr.2024.105396

Touma, D., Stevenson, S., Swain, D. L., Singh, D., Kalashnikov, D. A., & Huang, X. (2022). Climate change increases risk of extreme rainfall following wildfire in the western United States. *Science Advances*, *8*(13), eabm0320. https://doi.org/10.1126/sciadv.abm0320

Vaughn, N. R., Moskal, L. M., & Turnblom, E. C. (2012). Tree species detection accuracies using discrete point lidar and airborne waveform lidar. *Remote Sensing*, *4*(2), 377–403. https://doi.org/10.3390/rs4020377

Veraverbeke, S., Lhermitte, S., Verstraeten, W. W., & Goossens, R. (2010). The temporal dimension of differenced Normalized Burn Ratio (dNBR) fire/burn severity studies: The case of the large 2007 Peloponnese wildfires in Greece. *Remote Sensing of Environment*, *114*(11), 2548–2563. https://doi.org/10.1016/j.rse.2010.05.029

Wachter, C., Suter, J. F., Burkhardt, J., Austin, W., Haley, B. M., Pan, S., & Kolstoe, S. H. (2025). Characterizing community water systems exposed to wildfire in the Western U.S. *Science of the Total Environment*, *989*, 179814. https://doi.org/10.1016/j.scitotenv.2025.179814

Westerling, A. L. (2016). Increasing western US forest wildfire activity: Sensitivity to changes in the timing of spring. *Philosophical Transactions of the Royal Society B: Biological Sciences*, *371*(1696), 20150178. https://doi.org/10.1098/rstb.2015.0178

Williams, A. P., Abatzoglou, J. T., Gershunov, A., Guzman-Morales, J., Bishop, D. A., Balch, J. K., & Lettenmaier, D. P. (2019). Observed impacts of anthropogenic climate change on wildfire in California. *Earth's Future*, *7*(8), 892–910. https://doi.org/10.1029/2019EF001210

Wulder, M. A., White, J. C., Alvarez, F., Han, T., Rogan, J., & Hawkes, B. (2009). Characterizing boreal forest wildfire with multi-temporal Landsat and LIDAR data. *Remote Sensing of Environment*, *113*(7), 1540–1555. https://doi.org/10.1016/j.rse.2009.03.004

Yin, C., He, B., Yebra, M., Quan, X., Edwards, A. C., Liu, X., & Liao, Z. (2020). Improving burn severity retrieval by integrating tree canopy cover into radiative transfer model simulation. *Remote Sensing of Environment*, *236*, 111454. https://doi.org/10.1016/j.rse.2019.111454

Zhang, H., Huang, Q., Zhai, H., & Zhang, L. (2021). Multi-temporal cloud detection based on robust PCA for optical remote sensing imagery. *Computers and Electronics in Agriculture*, *188*, 106342. https://doi.org/10.1016/j.compag.2021.106342

Zhang, Q., Ge, L., Zhang, R., Metternicht, G. I., Du, Z., Kuang, J., & Xu, M. (2021). Deep-learning-based burned area mapping using the synergy of Sentinel-1&2 data. *Remote Sensing of Environment*, *264*, 112575. https://doi.org/10.1016/j.rse.2021.112575

Zheng, Y., & Fattahi, H. (2026). Modeling, prediction, and retrieval of surface soil moisture from InSAR closure phase. *Remote Sensing of Environment*, *333*, 115104. https://doi.org/10.1016/j.rse.2025.115104

Supplementary Files

This is a list of supplementary files associated with this preprint. Click to download.

- FigureS1samplingpoints.png
- FigureS1samplingpointsv2.png
- FigureS3bootstrapintervals.png